Enhancement of Si-Based Solar Cell Efficiency via Nanostructure Integration

Junshuai Li and Hong-Yu Yu

Abstract Solar cells are considered one of the most promising clean and renewable energy sources. Si wafer-based solar cells currently dominate the photovoltaic (PV) market with over 80% of the market share, largely owing to the available and rich manufacturing processes developed for the integrated circuit industry. However, the relatively high cost of the PV modules using Si wafer solar cells compared to conventional fossil fuels-based energy restricts its wide adoption for the civil electricity supply. How to effectively lower the costs of PV modules becomes one of the most important scientific and technical topics, especially considering the current world-wide efforts to combat climate change due to the "greenhouse" gas emissions when consuming carbon-based fossil energy. Two methodologies are generally pursued to realize this goal: one is to utilize low-grade raw materials and the other is by increasing the power conversion efficiency (PCE). In this chapter, the approaches to lower the costs and enhance the PCE of the Si-based solar cells by incorporating various Si nanostructures (e.g., nanodots, nanowires, nanocones and nanoholes) are presented, with details on the preparation techniques and their optical and electrical characteristics. The possible mechanisms of PCE improvement using these Si nanostructures are discussed in terms of enhanced light absorption and photogenerated carrier collection.

J. Li · H.-Y. Yu (✉)
School of EEE, Nanyang Technological University,
50 Nanyang Avenue, Singapore 639798, Singapore
e-mail: hyyu@ntu.edu.sg

L. Zang (ed.), *Energy Efficiency and Renewable Energy Through Nanotechnology*,
Green Energy and Technology, DOI: 10.1007/978-0-85729-638-2_1,

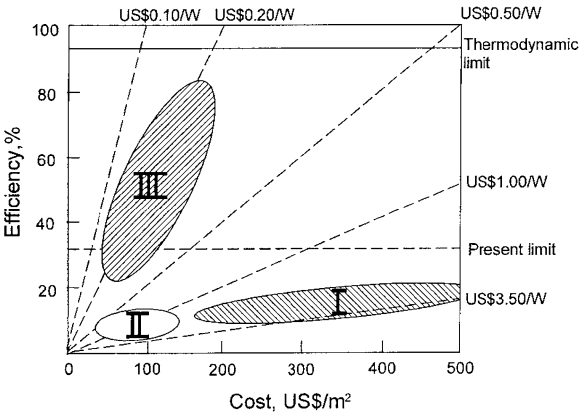

Fig. 1 Efficiency-cost trade-off for the three generations of solar cell technologies: wafers (region I), thin films (region II) and advanced thin films (region III). (Reprinted from Green [3], with permission from John Wiley and Sons; http://onlinelibrary.wiley.com/journal/10.1002/(ISSN)1099-159X)

1 Introduction

Nowadays, the negative impact of human activities to the environment receives tremendous attention, especially on the increased global temperature resulted from the emission of "greenhouse" gases such as CO_2 during production of carbon-based fossil energy. To combat climate change, clean and renewable energy sources need to be rapidly developed. Solar cell is considered as one of the ideal candidates, which directly converts solar energy into electricity without any "greenhouse" gas emissions [1].

At present, the first-generation solar cells based on Si wafers dominate, with more than 80% of the photovoltaic (PV) market [2]. However, the relatively high cost of Si wafer-based PV modules compared to other electricity sources severely restricts wide adoption of solar cells for civil utilities. To address this concern, both second and third generation solar cells are being actively pursued, as indicated in Fig. 1 [3]. Second generation solar cells are the thin film-based solar cells, which utilize inexpensive raw materials and cost-effective manufacturing techniques. Third generation solar cells are also under active research and introduce advanced physical concepts such as band gap engineering, down/up conversions for efficiently utilizing the ultraviolet/infrared photons, which are expected to significantly boost the power conversion efficiency (PCE) and reduce PV prices [4–6].

Among various materials and structures, Si-based nanostructures, such as nanodots (NDs) [7], nanowires (NWs) [8], nanocones (NCs) [9] and nanoholes (NHs) [10] are particularly promising for enhancing the PCE (and the cost per kilowatt hour) due to their unique optical and electrical properties. For example, the spectral response of the corresponding solar cells can be adjusted by incorporating SiNDs with different sizes [11], owing to quantum confinement effect on the energy gaps [12]. Accordingly, solar energy can be more efficiently utilized as compared to Si wafer solar cells with a fixed band gap ($\sim$1.12 eV). For Si-NWs,

the decoupling between the light trapping and photogenerated carrier collection enables the use of low-grade raw materials, which is beneficial to reducing the manufacturing cost without sacrificing the PCE [8, 13]. To date, the development of nanofabrication techniques has enabled researchers to prepare various nanostructures with controllable size, shape and spatial distribution in a low-cost manner, potentially leading to further cost reduction of the resultant PV modules. For example, Si-NDs have already been successfully prepared in SiO_2, Si_3N_4 and SiC matrix materials-based thin films by sputtering or plasma enhanced chemical vapor deposition (PECVD) followed by a post-annealing treatment [14–16]. Si-NWs, NCs, and NHs can also be produced in large areas, compatible with solar cell production via direct synthesis or dry/wet etching approaches [17–22].

In this chapter, the current research and development efforts on cell PCE enhancement via integration of these Si nanostructures are presented. The corresponding mechanisms to PCE improvement are also discussed.

2 Si Nanostructure-Based Solar Cells

Before turning to Si nanostructure-based solar cells, the energy losses in a standard single junction solar cell are briefly summarized. Figure 2 schematically illustrates the various energy loss processes [23]. When the incident light strikes solar cells, a portion of the photons are reflected back. For the photons entering the solar cells, only those with the energy above E_g (the energy band gap of the semiconductor materials) can be absorbed and generate electron–hole pairs. Those photons with the energy below E_g pass through the device without any contribution to the resulting PCE, as marked by process ①. For the photons absorbed by the solar cells, prior to extraction of the photogenerated electron–hole pairs to the load, the main energy loss occurs in process ②, i.e., the thermalization loss, which is due to the rapid thermal relaxation for the electron–hole pairs activated by high-energy (E) photons, in the form of releasing the energy of (E–E_g) to generate phonons. The other energy loss mechanisms include junction and contact voltage losses (③ and ④), and recombination loss ⑤. Both processes ① and ② account for $\sim$50% of the solar energy loss and are related to the fixed band gap of the semi-conductor (accordingly photons with too little or too much energy cannot be effectively utilized). To address these concerns, the multijunction (tandem) configuration is actively studied. PCE as high as $\sim$86.8% has been theoretically predicted for the multijunction configuration with an infinite stack of independently operated cells under direct sunlight exposure [5]. The Si-NDs system is an ideal candidate for the multijunction configuration due to its varied band gap value caused by the inclusion of dots with different sizes. The other design to efficiently utilize the high-energy photons is referred to as the "hot carrier" cell, where the idea is to quickly extract the "hot" carriers, i.e., the high-energy photogenerated carriers, before relaxation occurs [24]. To collect the "hot" carriers, the cell thickness must be thin due to the short carrier lifetime (less than $\sim$1 ps) [5].

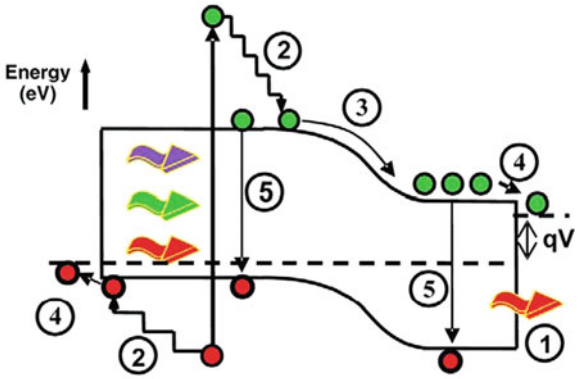

Fig. 2 Energy loss processes in a standard single junction solar cell: ① non-absorption of sub-band gap photons; ② thermalization loss; ③ and ④ junction and contact voltage losses; ⑤ recombination loss. (Reprinted from Conibeer [23], copyright 2007, with permission from Elsevier)

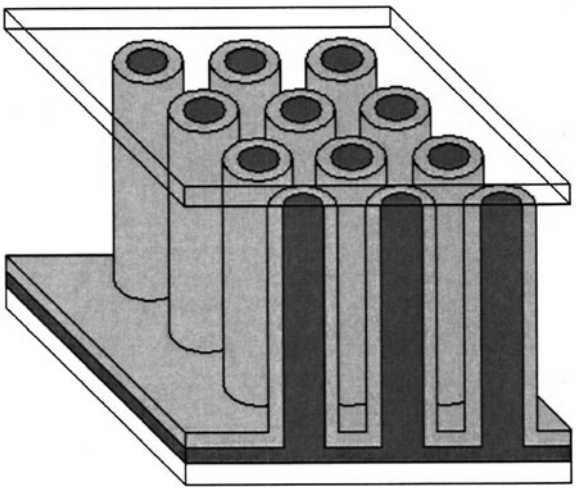

Fig. 3 Schematic of the radial p–n junction Si-NWs solar cell. Light is absorbed along the Si-NWs axis, the photogenerated carrier collection is along the radial direction of the Si-NWs. (Reprinted with permission from [8], copyright 2005, American Institute of Physics)

On the other hand, thin cell thicknesses are not able to absorb long-wavelength light. It is believed that this concern can be addressed through introducing the Si-NW, Si-NC and Si-NH structures, in which photogenerated carrier collection and light trapping can be decoupled, as shown in Fig. 3. Furthermore this type of solar cell design is beneficial to reduce the junction contact ③ and recombination losses ⑤ by controlling the Si nanostructure's dimension.

It is worth mentioning that the energy losses discussed above are only applicable to the absorbed and transmitted solar energy. The reflected portion is still considerable, which comes from the large difference of the refractive indices between air and solid Si [25]. An antireflection coating (ARC) can suppress light reflection to a certain extent; however, the effective light antireflection for the main energy range of the solar spectrum from $\sim$1 to 4 eV is challenging when using one layer of ARC with a low cost and without complicating the solar cell

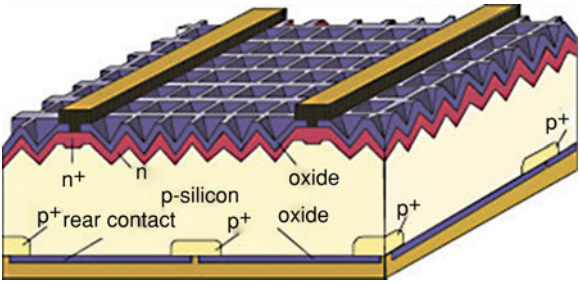

Fig. 4 Schematic of the state of the art Si wafer-based solar cell with "inverted pyramid" surface texture. (Reprinted from Green [29], with permission from John Wiley and Sons; http://onlinelibrary.wiley.com/journal/10.1002/(ISSN)1099-159X)

manufacturing [26]. For Si wafer-based solar cells, the well-known method to effectively reduce the light reflection is by surface texturing in micrometer scales, which elongates the optical path via multiple optical reflection [27, 28]. The state of the art Si wafer solar cell using the "inverted pyramid" surface texture (shown in Fig. 4) has demonstrated a PCE as high as 25.0%, and a short circuit current density of $\sim$42.7 mA/cm^2, which is $\sim$95% of the theoretical value of $\sim$45 mA/cm^2 (under the radiation condition of the revised AM 1.5G) [29]. However, the technique developed for Si wafer-based solar cells cannot be directly transferred to thin film solar cells due to thickness limitations. Fortunately, the nanoscale surface texturing by Si-NWs, Si-NCs and Si-NHs arrays can address this important issue. Different from microscale surface textured Si wafer solar cells, the mechanism for enhancing the light absorption in the Si nanostructure-textured thin film solar cells can be understood based on wave optics [30, 31]. More detailed discussion on this will be provided later in this chapter.

2.1 Si-Nanodot Solar Cells

2.1.1 Preparation of Si-NDs with Controllable Size

It is reported that Si-NDs can be prepared either by direct deposition using a PECVD system or by annealing sputtered or PECVD Si-rich oxides (SiO_{2-x}), nitrides (Si_3N_{4-x}) or carbides (SiC_{1-x}) [14–16]. The sizes of the Si-NDs can be controlled by adjusting the deposition parameters. In this section, both approaches are briefly discussed.

Figure 5 shows TEM images of samples of Si-NDs in silicon nitride matrices, which are deposited on p-type Si (100) wafers at a substrate temperature of 300°C using a conventional PECVD system [11]. Nitrogen-diluted 5% SiH_4 and NH_3 are used as the precursor gases, and the flow rate of SiH_4 is fixed at 190 sccm for all samples. For the samples shown in Fig. 5a–c, the working pressure during deposition is 1.0 Torr, and the flow rate of NH_3 increases from 10 to 90 sccm. The flow rate of NH_3 is 90 sccm for the sample shown in Fig. 5d and the working pressure is 0.5 Torr. It is clear that the Si-NDs' sizes are reduced by decreasing the flow ratio

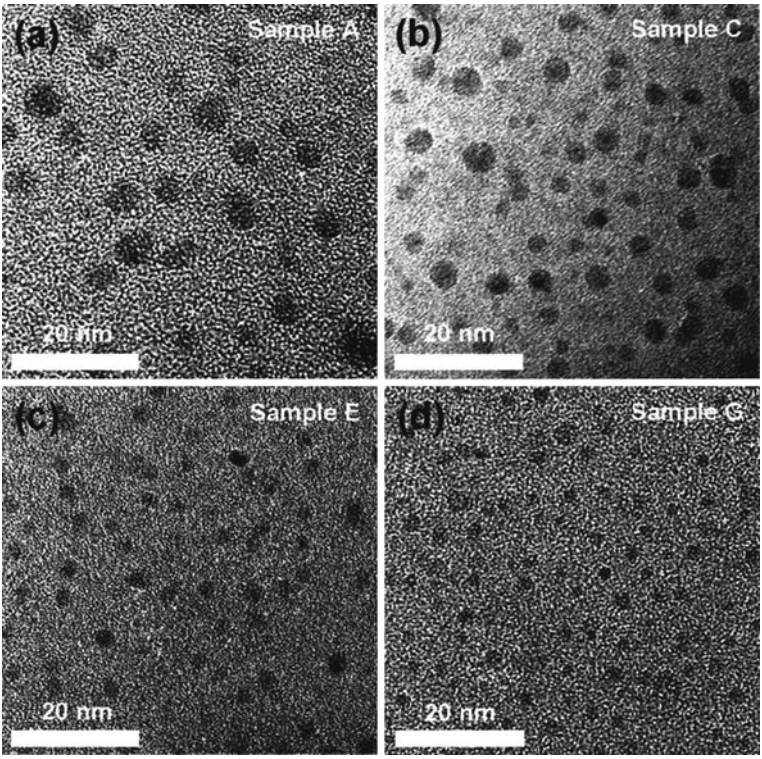

Fig. 5 TEM images of the in situ grown Si-NDs in the PECVD silicon nitride matrices. **a–c** The working pressure is 1 Torr, and the flow rate of NH_3 increases from 10 to 90 sccm. **d** The flow rate of NH_3 is 90 sccm, and the working pressure is 0.5 Torr. (Reprinted with permission from [11], copyright 2006, American Institute of Physics)

of SiH_4 to NH_3 and by decreasing the working pressure, demonstrating size control. The average diameters of the four samples are 4.9, 3.7, 3.2 and 2.9 nm, respectively. In this approach, the Si-NDs are formed during the gas phase transport process from the Si-contained radicals activated by plasma.

Different from the growth mechanism in the aforementioned direct deposition, the formation of Si-NDs through annealing Si-rich oxides follows the chemical reaction, as depicted in Eq. 1 [14]. Figure 6 shows the crystal size distribution and the corresponding plane-view TEM images after annealing the Si-rich oxide films, which were deposited using PECVD on Si (100) wafers at a substrate temperature of 300°C [32]. The precursor gases were SiH_4 (purity >99.99%) and N_2O. The crystal radius increases with an increasing annealing temperature from 1100 to 1250°C or increasing Si composition in the SiO_{2-x} films.

$$SiO_{2-x} \rightarrow \frac{x}{2}Si + \left(1 - \frac{x}{2}\right)SiO_2 \tag{1}$$

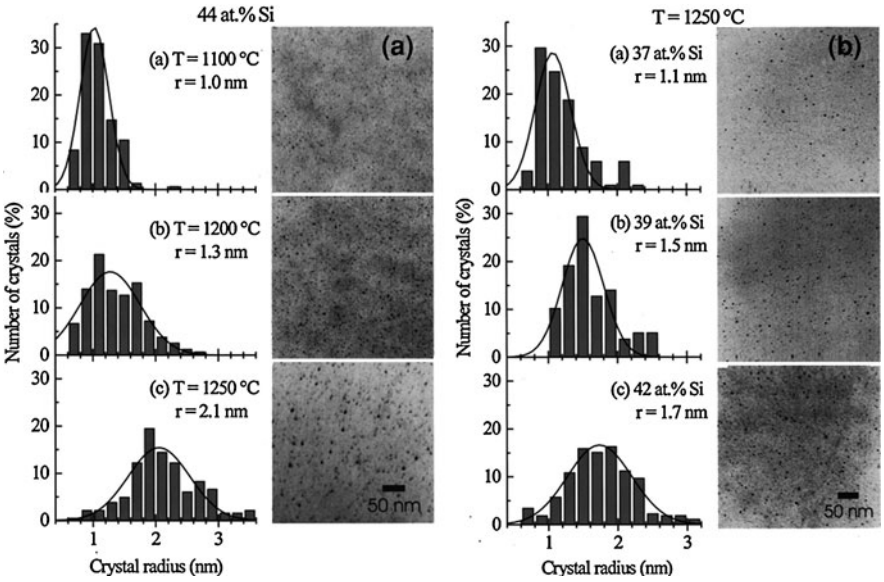

Fig. 6 Crystal size distribution and the corresponding plane-view TEM images for the Si-NDs prepared by furnace annealing the SiO_{2-x} films at different temperatures for 1 h at N_2 (**a**), and for the as-deposited films with various Si compositions at 1250°C for 1 h at N_2 (**b**). (Reprinted with permission from [32], copyright 2000, American Institute of Physics)

It was also reported that Si-NDs size can be controlled by forming a sandwich structure, such as $SiO_2/SiO_{2-x}/SiO_2$ [14, 33, 34]. Figure 7 shows cross-sectional TEM images of the SiO_{2-x}/SiO_2 superlattice before (a) and after (b) furnace annealing at 1100°C for 1 h in a N_2 atmosphere [14]. Amorphous SiO_{2-x}/SiO_2 is first prepared using reactive evaporation of SiO powders in an oxygen atmosphere with a Si-wafer substrate temperature of 100°C. The thickness of SiO_{2-x} or SiO_2 single layer is $\sim$2.8–3.2 nm for the as-prepared sample, as indicated in Fig. 7a. After furnace annealing, the Si-NDs are segregated in the Si-rich SiO_{2-x} layers, and confined by the adjacent SiO_2 layers, as shown in Fig. 7b. The mean size estimated from TEM measurements is 3.3 ± 0.5 nm, consistent to the original thickness of the SiO_{2-x} layers. For this approach, it should be noted that the thickness of the Si-rich layers should not exceed 4 nm to achieve uniform size distribution of the Si-NDs. Otherwise, the precipitation of Si atoms will transit from the two-dimensional (2D) diffusion to 3D diffusion, resulting in a wider size distribution [7].

2.1.2 Optical and Electrical Characteristics of Si-NDs in Dielectric Matrices

As mentioned earlier, the energy band gap of Si-NDs is tunable, owing to the quantum confinement effect, and this implication is important for solar cell

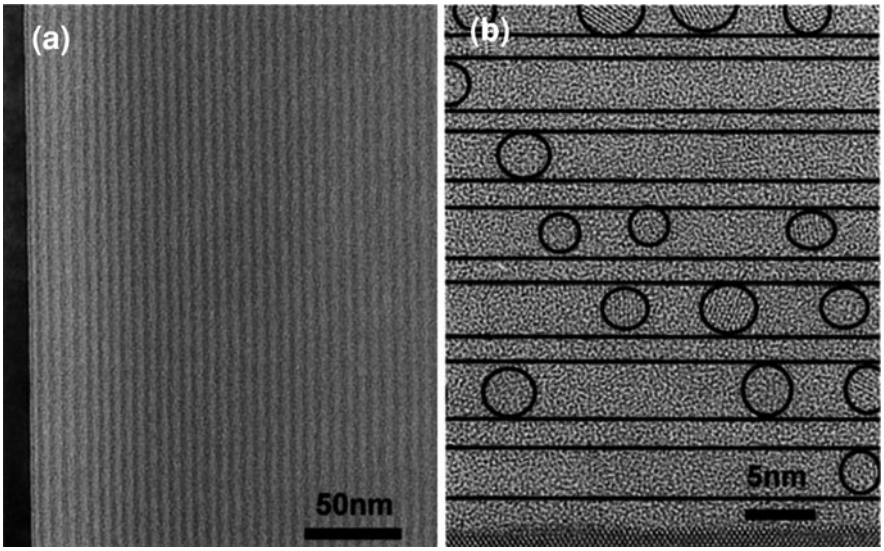

Fig. 7 TEM images of the SiO_{2-x} ($x \sim 1$)/SiO_2 superlattices: **a** as-prepared superlattice (the darker regions indicate the SiO_{2-x} sublayers); **b** the same sample after annealing at 1100°C for 1 h under N_2 atmosphere. (Reprinted with permission from [14], copyright 2002, American Institute of Physics)

applications. It favors the selective absorption of photons with different energies to minimize the energy relaxation of "hot" carriers, hence boosting the resultant PCE. Accordingly, understanding how the optical and electrical characteristics depend on Si-NDs size and distribution is necessary to guide material preparation and structure design for solar cells based on this technology. In this section, the optical and electrical characteristics of Si-NDs in various dielectric matrices are introduced, with emphasis on solar cell applications.

The optical characteristics of Si-NDs directly depend on the effective band gap, which is further determined by the Si-NDs size and the surrounding matrix [7]. Note that the band structure of the Si-NDs becomes almost direct when the Si-NDs' sizes are small enough (in general, this value should be below 7 nm for quantum confinement effect to dominate) [7]. Figure 8 shows the room temperature photoluminescence (PL) spectra of the Si-NDs, which are grown in situ in the silicon nitride films using PECVD with 10% SiH_4, diluted in argon and pure (>99.9999%) NH_3, on Si (100) wafers at 250°C [35]. It is interesting that the peak position in the PL spectra can be modulated from infrared to ultraviolet with decreasing size of the Si-NDs. By correlating the size distribution of the Si-NDs with the corresponding PL peak, the relationship between the Si-ND size and band gap (Fig. 9) can be empirically established, which is described by Eq. 2:

$$E = 1.16 + \frac{11.8}{d^2}, \tag{2}$$

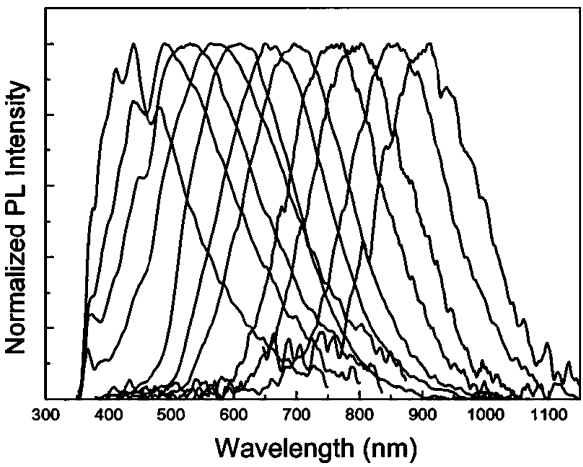

Fig. 8 Room temperature PL spectra of the Si-NDs grown in situ in silicon nitride films. (Reprinted with permission from [35], copyright 2004, American Institute of Physics)

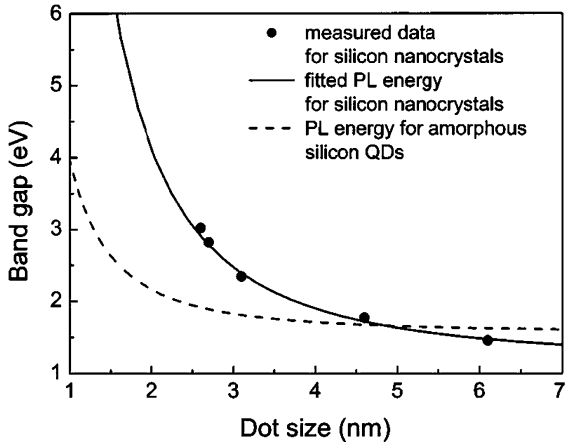

Fig. 9 PL peak energy of Si-NDs grown in situ in silicon nitride films as a function of dot size. The *solid line* indicates the energy band gap calculated using Eq. 2. (Reprinted with permission from [35], copyright 2004, American Institute of Physics)

where E is the band gap in eV and d is the Si-ND's diameter in nm.

Here it should be mentioned that Eq. 2 is based on effective mass theory with the assumption of an infinite potential barrier [35]. A more commonly used expression is shown in Eq. 3 [36]:

$$E = E_{\text{bulk}} + \frac{C}{d^2}, \tag{3}$$

where E and E_{bulk} are the energy band gaps of the NDs and the bulk material (with the same composition as the NDs) in eV, d is the ND's diameter in nm, and C is the confinement parameter. For different materials and surrounding environments, the effect on the energy band gap can be reflected by the variation in E_{bulk} and C. Figure 10 summarizes the values of the band gap of Si-NDs in silicon oxide and nitride matrices from PL measurements [7]. The data follows the trend

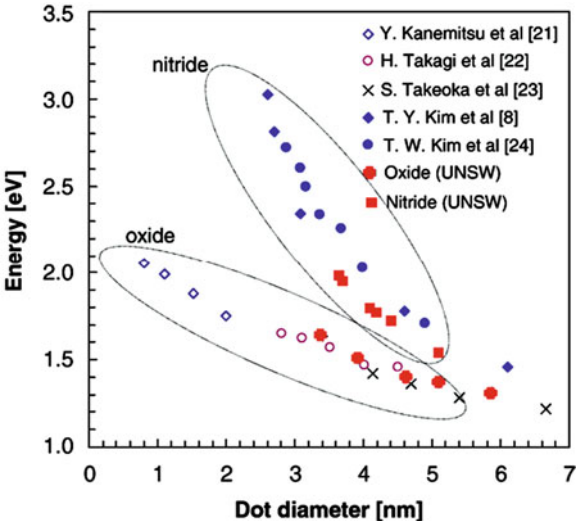

Fig. 10 Energy band gap of Si-NDs in silicon oxide and nitride matrices as a function of the Si-ND's diameter. The data are summarized from the PL measurements performed by different groups (note that the reference numbers marked in this figure given in [7]). (Reprinted from Conibeer [7], copyright 2008, with permission from Elsevier)

depicted by Eq. 3, and the sharp increase in band gap with decreasing diameters indicates the strong quantum confinement effect in Si-NDs in silicon nitride films.

To achieve high efficiencies in solar cells, both effective utilization of the incident photons and the efficient collection of the photogenerated carriers are important. Different from a standard Si wafer-based solar cell, the carrier transport in Si-ND solar cells strongly depends on tunneling between the neighboring dots through a barrier formed by the matrix materials.

The transmission probability (T) of a carrier between the two states with the same level can be approximated by a simplified formula [37]:

$$T \approx 16 \exp\left\{-d\sqrt{\frac{8m^*}{\hbar^2}\Delta E}\right\}, \tag{4}$$

where d is the barrier width, i.e., the spacing between the neighboring dots, m^* is the effective mass of the carrier, ΔE is the energy difference between the conduction band edges (for electrons) of the matrix material and the Si-NDs, or between the energy level in the Si-NDs and the valence band edge (for holes) of the matrix material, and $\hbar$ is the reduced Plank constant. It is obvious that the transmission probability exponentially decreases with increasing $\left[d(m^*\Delta E)^{1/2}\right]$. Figure 11 schematically illustrates the energy band diagram for bulk Si in contact with SiC, Si_3N_4 and SiO_2 [6]. Among SiO_2, Si_3N_4, and SiC, the energy band offset between bulk Si to SiC is smallest, indicating an enhanced T for Si-NDs embedded in SiC. On the other hand, it is also noted that the formation of Si-NDs in SiC is more challenging than in SiO_2 due to the weak polarity or Si–Si length in Si-rich carbides. As indicated in Eq. 4, another way to increase T is by reducing the Si-NDs' size, which increases the energy level of carriers in Si-NDs and therefore

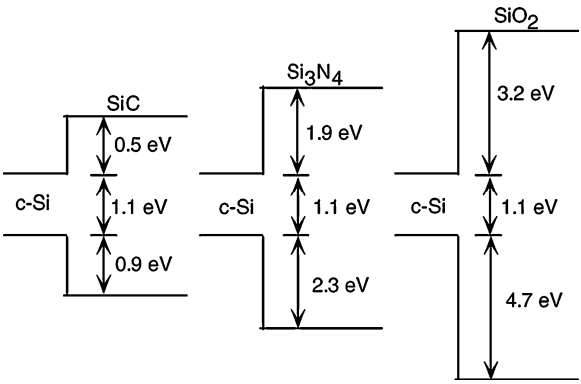

Fig. 11 Schematic of the energy band diagrams for bulk Si contacted to SiC, Si_3N_4 and SiO_2. (Reprinted from Conibeer [6], copyright 2006, with permission from Elsevier)

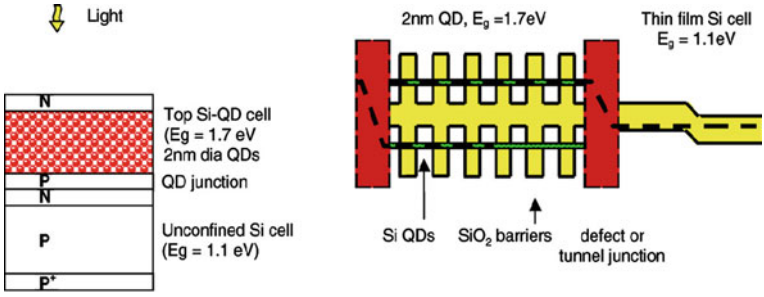

Fig. 12 Schematic of a Si-based tandem solar cell with a Si-ND *top* cell and a Si *thin* film *bottom* cell (*left*), and the energy band diagram of the tandem solar cell (*right*). (Reprinted from Conibeer [7], copyright 2008, with permission from Elsevier)

decreases ΔE. Last but not least, to enhance the resonance tunneling current, uniform size among all Si-NDs is a key factor, supported by theoretical calculations [38]. For the tunneling distance d between neighboring Si-NDs, a slight variation does not have significant impact on T.

2.1.3 Research Status of Si-ND-Based Solar Cells

Figure 12 schematically shows the structure of a typical Si-ND-based tandem solar cell, consisting of a Si-ND-based top cell and a Si thin film-based bottom cell [7]. Due to quantum confinement, the energy band gap of $\sim$1.7 eV is achieved for Si-NDs with the diameter of $\sim$2 nm in the SiO_2 matrix, as indicated in Fig. 10. This cell can capture the photons with the energies greater than 1.7 eV and convert them into photogenerated carriers. Photons with the energies below 1.7 eV pass through and are absorbed by the bottom cell. The expected overall efficiency is enhanced. As shown in Fig. 13, the efficiency of this tandem cell can reach $\sim$35%,

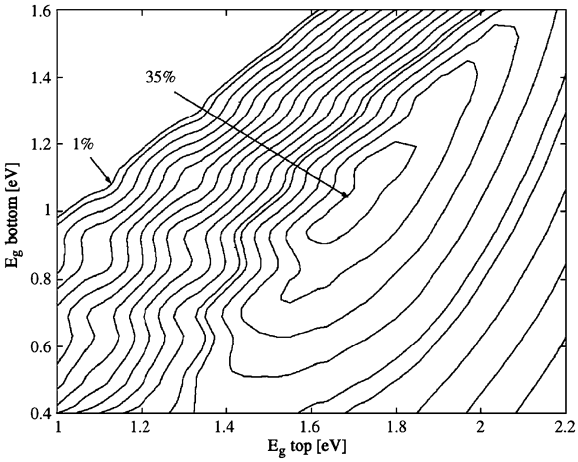

Fig. 13 Upper limit of the efficiency of p–i–n/p–i–n tandem solar cell as a function of the energy gaps $E_{g,top}$ and $E_{g,bottom}$. (Reprinted from Meillaud [39], copyright 2006, with permission from Elsevier)

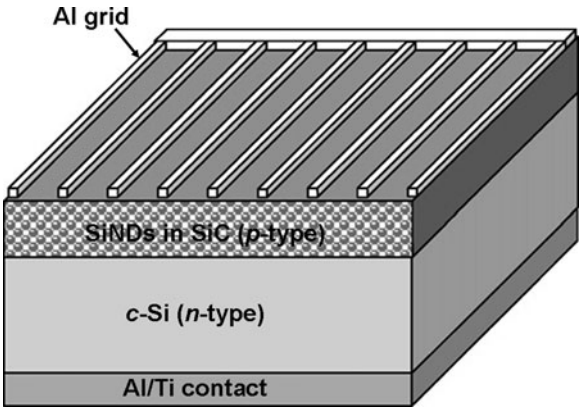

Fig. 14 Schematic of a p-type Si-NDs layer/n-type Si wafer heterojunction solar cell. (Reprinted from Song et al. [40], copyright 2008, with permission from Elsevier)

which is an improvement over the 29% calculated for a single junction Si wafer solar cell [39].

Currently, Si-ND-based solar cells are still in the early phase of research [40–44], with the majority of the work concentrating on the preparation and optical/electrical characterization of high quality materials with controllable size and/or size distribution. Thus, only preliminary experimental results related to the Si-ND layer/Si wafer heterojunction devices are summarized in this section, which is followed by guiding proposals to manufacture high efficiency Si-NDs-based solar cells.

Figure 14 shows the schematic of a typical Si-ND layer/Si wafer heterojunction device [40]. The top layer ($\sim$0.8 μm thick) is an Al metal grid, which serves as the top electrode, permitting incident light to pass through and forming an Ohmic contact with the underlying p-type Si-ND layer. The p-type Si-ND layer with Si-ND diameters of $\sim$3–5 nm is prepared by annealing the $Si_{1-x}C_x/SiC$ $(x \sim 0.1-0.15)$ multilayers at 1100°C for 9 min in a N_2 environment and are

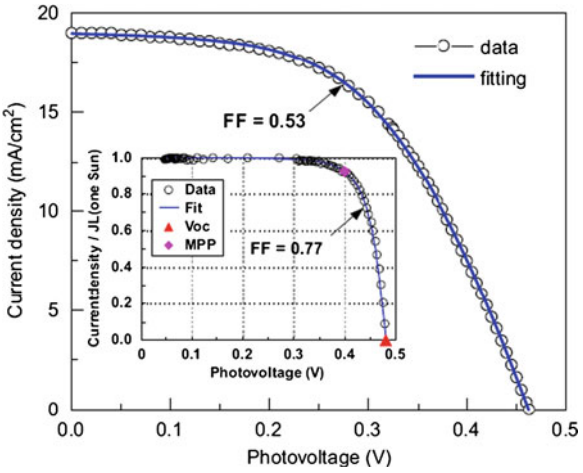

Fig. 15 Illuminated *I–V* curve of a p-type Si-ND layer/n-type Si wafer heterojunction solar cell under AM 1.5G. The *solid line* indicates a fitting curve using a two-diode model. The *inset* shows the pseudo *I–V* without considering the series resistance. (Reprinted from Song et al. [40], copyright 2008, with permission from Elsevier)

deposited using magnetron co-sputtering from Si and SiC targets (the SiC target is boron-doped). The respective thicknesses of the as-deposited $Si_{1-x}C_x$ and SiC layers are ~6 and ~2.5 nm, and the total thickness is ~160 nm. After annealing and dopant activation, the resulting Si-ND layer has a resistivity of $\sim 10^{-1}$–10^{-2} Ω cm. The resistivity of the n-type Si (100) wafer is ~2–9 Ω cm (a doping concentration of ~ 0.4–2.5×10^{15} cm^{-3}). The Ohmic back contact is built by evaporating a layer of 30 nm thick Ti film, followed by a 1.0 μm-thick Al layer. It is worth noting that there is no surface texturing or antireflection coating in the resulting solar cells.

Figure 15 shows the illuminated *I–V* characteristics of the above heterojunction solar cell at the standard AM 1.5G, i.e., the illumination condition of 100 mW/cm^2 at 25°C. The open circuit voltage, V_{oc}, short circuit current density, J_{sc} and fill factor are ~463 mV, 19 mA/cm^2 and 0.53, respectively, resulting in a PCE of ~4.66%. From the comparison with the pseudo *I–V* curve obtained by the *Suns-*V_{oc} method without considering the series resistance (shown in the inset of Fig. 15), the degradation of the fill factor is mainly attributed to the high series resistance, ~4.72 Ω cm^2, which probably comes from the imperfect Ohmic contact between the top electrode and the Si-ND layer. The low V_{oc} is due to carrier recombination, especially in the junction region, which is reflected by the relatively high ideality factor of ~1.24 extracted from the dark *I–V* measurement in the intermediate bias voltage of ~0.1–0.4 V. Meanwhile, the high light reflection (as shown in Fig. 16) of the solar cell leads to the lower external quantum efficiency (EQE) and J_{sc} compared to the surface-textured devices. One notes that the internal quantum efficiency (IQE) in the high-energy region of the solar spectrum, such as ~400 nm, is higher than that of the conventional Si wafer solar cell, which is attributed to the enlarged energy gap of the Si-ND layer. The following results validate this statement [41].

Devices consisting of an n-type Si-NDs layer/p-type Si (100) wafer (resistivity ~5–20 Ω cm) heterojunction were also prepared [41]. Si and SiO_2 targets were used

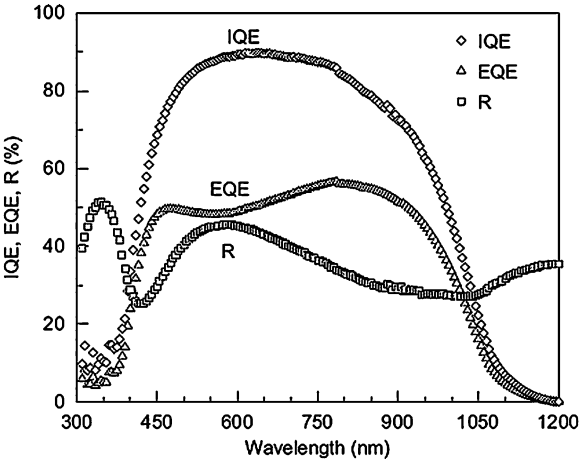

Fig. 16 Reflectance (R), external quantum efficiency (EQE) and internal quantum efficiency (IQE) for the same solar cell shown in Fig. 15. (Reprinted from Song et al. [40], copyright 2008, with permission from Elsevier)

Table 1 Parameters of the illuminated n-type SiNDs layer/p-type Si wafer heterojunction solar cells at AM 1.5G, i.e., ~100 mW/cm^2 at 25°C

No.	Thickness and number of $SiO_{0.89}/SiO_2$ multilayers	V_{oc} (mV)	J_{sc} (mA/cm^2)	FF (%)	PCE (%)
1	3 nm/2 nm, 15	555.6	29.8	63.8	10.6
2	4 nm/2 nm, 25	540.3	25.0	76.8	10.4
3	5 nm/2 nm, 25	517.9	27.9	72.3	10.5
4	8 nm/1 nm, 25	470.8	18.6	65.1	5.7

Reprinted with permission from [41], copyright 2008, Institute of Physics

to deposit $SiO_{0.89}$ and SiO_2 multilayers, and a P_2O_5 target was utilized for n-type doping in the Si-rich oxide layers. Si-ND formation and dopant activation were accomplished by the furnace annealing at 1100°C for 1.5 h in a N_2 environment. Al electrodes were evaporated on the top (via a shadow mask) and bottom of the solar cells, and then annealed at 400°C for 30 min in N_2 to improve the contact.

The electrical parameters of the solar cells with $SiO_{0.89}/SiO_2$ multilayers with varying thicknesses are collected under the illumination condition of AM 1.5G and summarized in Table 1. It is worth noting that V_{oc} increases with decreasing thickness of the $SiO_{0.89}$ sublayer, in line with the resulting size of the Si-NDs. It is believed that the enlarged energy band gap of the Si-ND layer with the decreased $SiO_{0.89}$ thickness can be correlated to the increased V_{oc}. It is also seen that the J_{sc} for device-1, with the thinnest Si-ND layer, is highest, indicating that the majority of photocurrent is not from this layer. As the thickness of the Si-ND layer increases, the larger tunneling distance coupled with the accumulated defects in this layer leads to the reduction of J_{sc}.

Figure 17 shows the IQE curves for the four samples. It is clearly shown that the IQE is reduced in the high-energy region with the increase of the Si-NDs' size, and the peak shifts toward low energy (or long wavelength). This figure provides

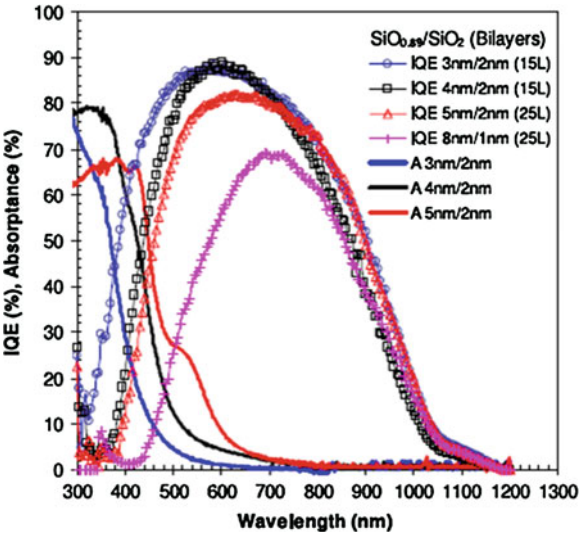

Fig. 17 IQE of the n-type SiNDs layer/p-type Si wafer heterojunction solar cells with different thicknesses and numbers of the $SiO_{0.89}/SiO_2$ multilayers. The light absorption of the SiNDs layer for the first three devices is also included. (Reprinted with permission from [41], copyright 2008, Institute of Physics)

evidence that the enlarged energy band gap for the SiNDs layer leads to the higher IQE for the Si-ND layer/Si wafer heterojunction solar cell in the higher energy region of the solar spectrum compared to the Si wafer homojunction devices [40]. As seen from the same figure, the light absorption in the Si-NDs layers mostly occurs in the high-energy region of the solar spectrum. With the increase of Si-ND size, the absorption edge shifts toward the low-energy regime due to the decrease in the effective band gap.

Following the brief summary of the current research efforts on SiNDs layer/Si wafer heterojunction solar cells, some guidelines to achieve the high-efficiency and cost-effective Si-ND-based solar cells are proposed below:

(i) *Close-packed Si-NDs with uniform size distribution*. To efficiently collect photogenerated carriers, the Si-NDs must be closely packed for the high resonant tunneling efficiency between the neighboring Si-NDs. On the other hand, how to prepare close-packed Si-NDs by controlling the nucleation sites is not only critical, but challenging.

(ii) *Effective high doping of the Si-NDs layer*. The doping of Si-NDs is difficult from the aspects of energy and kinetics due to small-size effects [45, 46]. To realize a high-quality p–n junction for effectively extracting the photogenerated carriers, high-dose doping in the Si-NDs emitters is necessary.

(iii) *High-quality Ohmic contact with the Si-ND layer*. As discussed previously, the series resistance severely affects the illuminated *I–V* curve by decreasing the fill factor. Accordingly, exploring suitable metal electrodes and metallization process is highly demanded.

(iv) *Optimized conjunction between neighboring cells*. The low V_{oc} for the above devices results from carrier recombination, especially in the conjunction regions, can be attributed to the defects created during high-temperature

annealing and the different thermal expansion factors of the various materials. Optimizing the conjunction by employing low-temperature processes is desirable for lowering the defect density.

(v) *Antireflection design for suppressing light reflection*. It is clear that the light reflection is another major source of loss in the aforementioned devices, evidenced by their low EQEs. Therefore, an appropriate surface texturing or antireflection coating is also essential for high-efficiency Si-ND-based solar cells.

2.2 Stand-Alone Si Nanowire-Based Solar Cells

2.2.1 Preparation of Si-NWs Array with Controllable Dimension

As one of the fundamental building blocks of the "nanoworld", Si-NWs have been extensively studied in recent years [47–53]. The methods to prepare Si-NWs can generally be categorized into two classes: one is the "top-down" method [54, 55] and another is the "bottom-up" approach [56, 57]. The former commonly involves preparing Si-NWs using various etching methods or combining different patterning techniques. The latter case is generally based on the vapor–liquid–solid (VLS) mechanism [58] to grow Si-NWs with the assistance of various catalysts such as Au, Cu, Fe, Al, etc. [59–62]. On the other hand, it needs to be pointed out that neither approach is perfect. For instance, by using the reactive ion etch (RIE) with electron beam or photolithography, one can fabricate highly uniform Si-NWs, which are commonly used in integrated circuit devices such as transistors [63, 64]. However, the high cost/low throughput of such a process strictly restricts its application in solar cell industry. The VSL growth of Si-NWs with an area of over 1 cm^2 can be realized even on glass substrates [17]. However, the unavoidable doping from the catalysts during growth can introduce deep energy level defects, which severely affect the electrical characteristics of the resulting Si-NWs [65]. On the other hand, for solar cell applications, the critical factor to be considered for the preparation of Si-NWs is the cost. With low costs, efficient light trapping and photogenerated carrier collection also needs to be studied. In this section, we highlight the approaches to prepare the Si-NWs with low costs and high controllability in terms of dimension and spatial distribution.

Electron beam or photolithography is acknowledged as a key factor leading to the high cost of preparing Si-NWs for solar cell applications. The alternative patterning methods to replace them have been actively pursued. Recently, the Cui group from Stanford University reported using a Langmuir–Blodgett (LB) [66] assembled monolayer of the SiO_2 particles to serve as the "nanosphere" lithographic mask. Using this approach, uniform and dense patterning can be achieved over a large area as shown in Fig. 18 [19].

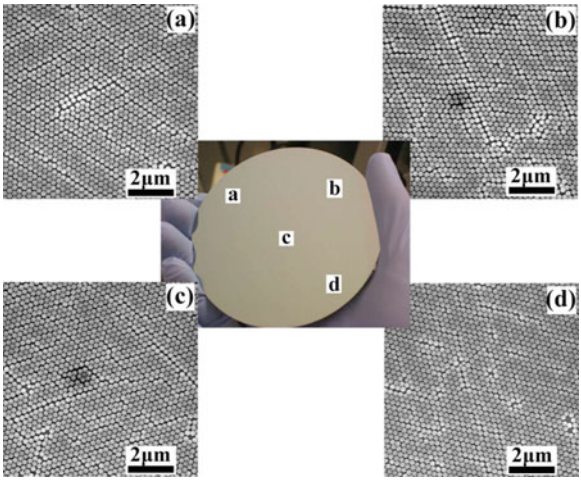

Fig. 18 SEM images of the close-packed SiO_2 nanosphere (diameter of ~200 nm) monolayer prepared by the Langmuir–Blodgett method on a 4 in. Si (100) wafer. Figures **a**–**d** demonstrate the four different regions corresponding the symbols marked in the wafer, indicating a high uniformity over the large area. (Reprinted with permission from [19], copyright 2008, American Institute of Physics)

After forming the close-packed SiO_2 nanosphere monolayer, reactive ion etching (RIE) can be performed to selectively reduce the dimension of the SiO_2 nanospheres using O_2 and CHF_3, as demonstrated in Fig. 19a, b [19]. Then Cl_2-based RIE is used to anisotropically etch away the underlying Si material with SiO_2 nanospheres acting as a hard mask, creating a highly-ordered Si-NWs array (see Fig. 19c). The residual SiO_2 at the tip of the Si-NWs can then be removed by HF acid. Figure 19d shows the tilted SEM image of the resulting Si-NWs array. It is clear that the array's periodicity is transferred from the SiO_2 nanospheres in the as-prepared monolayer. The Si-NWs' diameters can be modulated by adjusting the RIE parameters. Moreover, the dimension of the Si-NWs can be further scaled to below 100 nm with additional thermal oxidation and subsequent HF etching. It is worth mentioning that this approach can be utilized to manufacture Si-NWs arrays on polycrystalline Si or amorphous Si thin films [9].

Except the RIE method, which requires relatively expensive equipment, another more cost-effective wet etching approach has also been used to fabricate high-quality Si-NWs arrays [67]. Figure 20 shows the schematic process flow and the corresponding SEM images in preparing a highly-ordered Si-NWs array using electroless wet etching to replace the anisotropic RIE. Si wafers are first cleaned in a boiled solution of NH_4OH: H_2O_2: H_2O = 1:1:5 for 1 h to achieve a hydrophilic surface. The close-packed SiO_2 nanosphere monolayer is then prepared via the method described by Lu et al. [68] from a SiO_2 colloidal solution, as shown in Fig. 20a. The SiO_2 nanospheres' dimensions can be reduced by chemical etching in HF solution (see Fig. 20b). This is followed by catalyst metal deposition, such as Ag or Au, using vacuum evaporation. The area on the Si wafer not covered by SiO_2 nanospheres is exposed to the catalyst metal layer as shown in Fig. 20c. After removing the SiO_2 nanospheres by ultrasonication in water for 2–3 min, the metal thin film with the periodic nanopore array is achieved (see Fig. 20d). After immersing the sample into the HF/H_2O_2 solution, the highly-ordered Si-NWs array was created by the selective electroless etching of the Si underneath the catalyst metal, as observed in Fig. 20e. The Si-NWs' length can be easily adjusted by

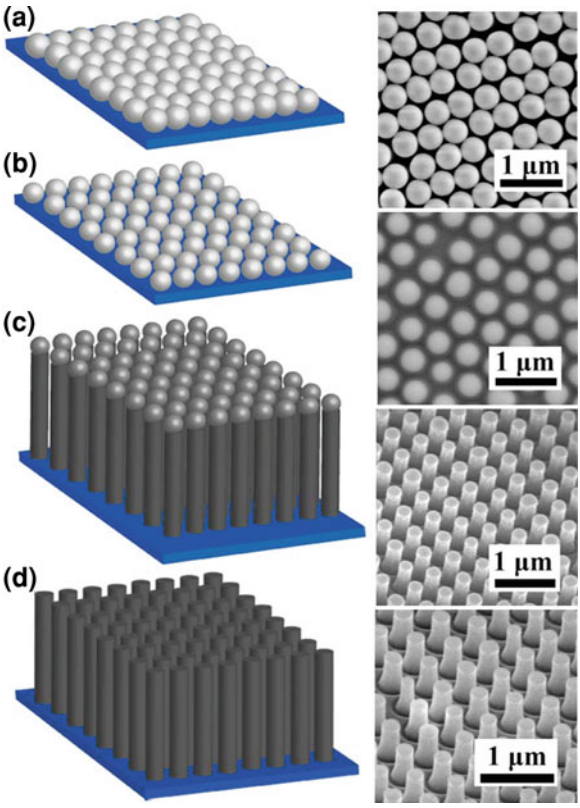

Fig. 19 Schematic (*left*) and the corresponding SEM image (*right*) of each step used to prepare a highly-ordered Si-NW array with the controllable periodicity and Si-NW diameter using RIE combined with the SiO_2 nanosphere Langmuir–Blodgett patterning method. **a** Deposition of the silica nanoparticles by Langmuir–Blodgett. **b** Shrinking of the mask by isotropic RIE of SiO_2. **c** Anisotropic etching of Si into pillars by RIE. **d** Removal of the residual mask by HF etching. (Reprinted with permission from [19], copyright 2008, American Institute of Physics)

changing the etching time, and the array's periodicity and Si-NWs diameter are controlled by the diameters of the starting and reduced SiO_2 nanospheres. In general, the etching mechanism is based on the following chemical processes [69]:

With Ag nanoparticles:

$$H_2O_2 + 2H^+ \rightarrow 2H_2O + 2h^+,$$

$$2H^+ + 2e \rightarrow H_2 \uparrow,$$

With Si:

$$Si + 4h^+ + 4HF \rightarrow SiF_4 + 4H^+,$$

$$SiF_4 + 2HF \rightarrow H_2SiF_6,$$

Overall reaction:

$$Si + H_2O_2 + 6HF \rightarrow 2H_2O + H_2SiF_6 + H_2 \uparrow .$$

There are also other approaches based on the "top-down" paradigm to create Si-NWs arrays. Generally speaking, to integrate Si-NWs arrays in solar cells, the

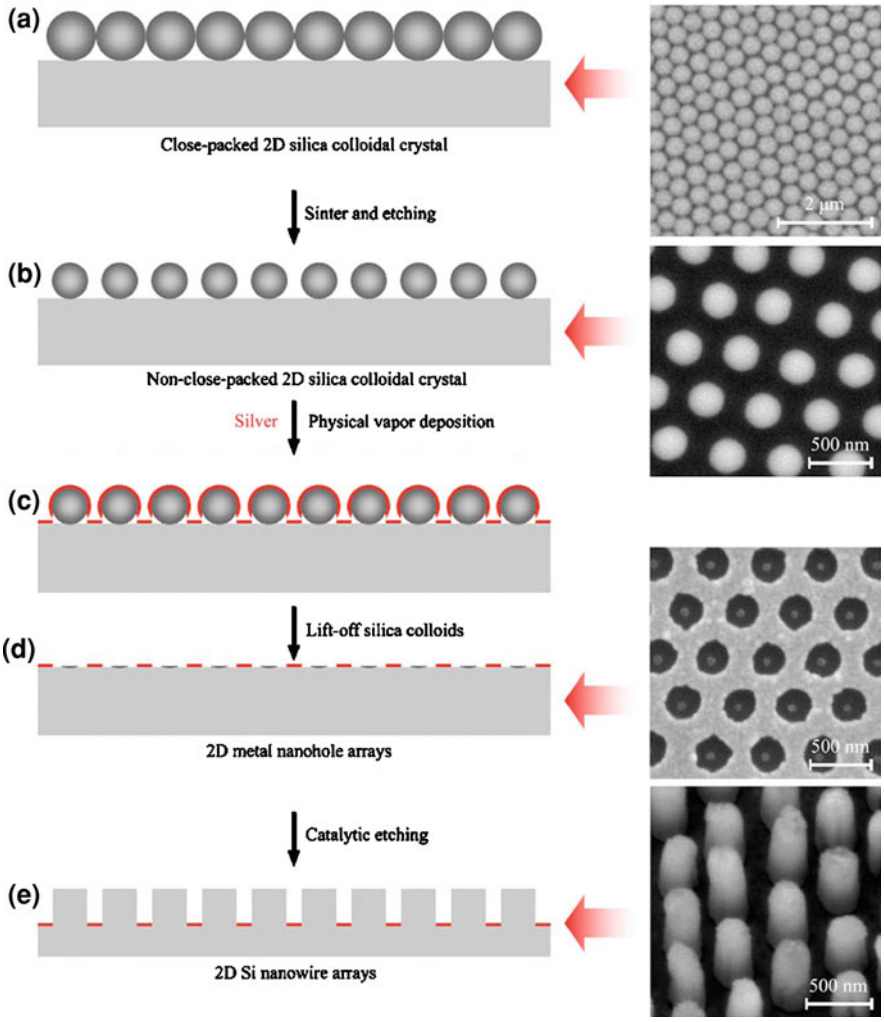

Fig. 20 Schematic of the process flow (*left*) and the corresponding SEM image (*right*) of each step used in preparing a highly-ordered Si-NW array with controllable periodicity and diameter using electroless etching combined with a self-assembled SiO_2 nanosphere monolayer severing as the mask. **a** Deposition of monolayer silica colloidal crystal template on silicon surface; **b** fabrication of 2D non-close-packed silica colloidal crystals on silicon surface; **c** deposition of silver layer on silicon surface through the non-close-packed colloidal crystal template; **d** formation of regular silver nanohole arrays by removing silica colloids by brief ultrasonication in water; and **e** formation of Si-NWs by catalytic etching. The corresponding SEM micrographs on the right show the monolayer silica colloidal crystal template (**a**), the 2D nonclose-packed silica colloidal crystal template (**b**), the silver film with periodic nanohole arrays (**d**), and ordered Si-NW arrays produced using catalytic silver film with periodic nanoholes (**e**). (Reprinted with permission from [67], copyright 2007, American Institute of Physics)

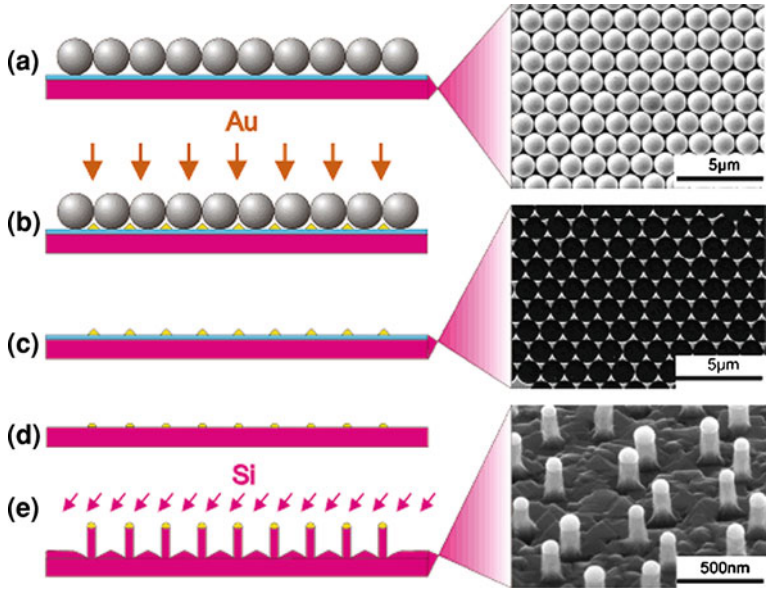

Fig. 21 Schematic of the process flow (*left*) and the corresponding SEM image (*right*) to prepare highly-ordered Si-NW arrays with controllable spatial distribution and size using VLS-based "bottom-up" growth combined with a pre-patterned Au catalyst. **a** Deposition of a mask of polystyrene particles on a Si-(111) substrate covered by a 2-nm-thick oxide layer (*blue*), **b** deposition of gold by thermal evaporation, **c** removal of the spheres, **d** thermal annealing and cleaning step to remove the oxide layer, and **e** Si deposition and growth of nanowires by MBE. The first two SEM images correspond to the use of PS nanospheres having the diameter of ~1320 nm, and the third corresponds to the PS nanospheres with the diameter of 600 nm. (Reprinted with permission from [70], copyright 2005, American Chemical Society)

trade-off between the manufacturing cost and the enhanced PCE should be seriously taken into account.

Next let us turn to the "bottom-up" approaches to grow Si-NWs arrays. Through manipulating the spatial and size distribution of the catalysts, the controllable periodicity and diameter can be achieved using the VLS paradigm. Because VLS growth itself is cost-effective, the final manufacturing cost strongly depends on the lithographic process to pattern the catalysts. Here several low-cost lithographic processes are discussed.

Figure 21 illustrates an example process to prepare a Si-NWs array by the VSL-based "bottom-up" technique [70]. Similar to the patterning process used in the aforementioned "top-down" etching technique, a close-packed monolayer of polystyrene (PS) nanospheres with desired diameters is deposited by spin coating, as shown in Fig. 21a. Then, an Au layer with a thickness between 10 and 20 nm is deposited via thermal evaporation. Au nanoislands on the substrate are formed due to the triangular interspacing between neighboring PS nanospheres, as demonstrated in Fig. 21b. After clearing the PS nanospheres by ultrasonication in CH_2Cl_2 for 2 min, the well-arranged Au nanoislands with a hexagonal pattern are formed

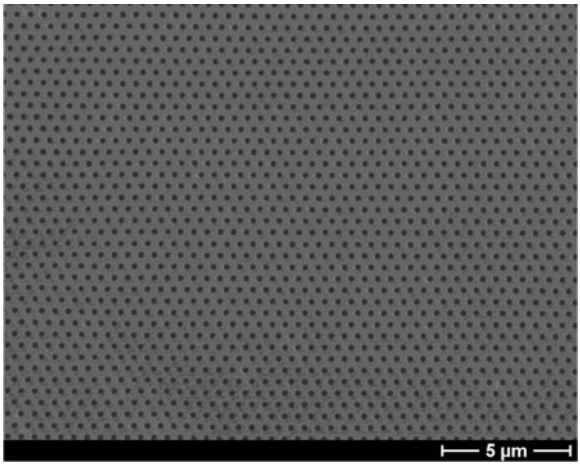

Fig. 22 Plane-view SEM image of monodomain AAO with a pore diameter of 180 nm and interpore distance of 500 nm. (Reprinted with permission from [73], copyright 2003, American Chemical Society)

(see Fig. 21c). The sample can be transferred to the Si-NWs growth system, an ultrahigh vacuum MBE chamber in this example. The sample is heated to 810°C for 10 min to transform the triangular Au nanoislands into hemispheres as schematized in Fig. 21d. Then the Si-NWs growth is performed at a sample temperature of 525–570°C. The Si-NWs' lengths are controlled by the deposition time. As indicated in Fig. 21e, the resulting Si-NWs array transfers the pattern from the hexagonal Au nanoparticles. The spatial distribution and diameter of the Si-NWs can be modulated by varying the diameter of the PS nanospheres and the thickness of the Au film.

Anodic aluminum oxide (AAO) with hexagonally arranged nanopores (see Fig. 22) has been widely utilized in preparing aligned arrays of various nanostructures of different materials [71–74]. AAO can be manufactured using the electrochemical anodization of pure aluminum over a large area based on the dissipation structure mechanism [75]. The nanopore size and spacing can be tuned by adjusting the electrochemical anodization conditions. For instance, the nanopore size and density can be controlled by varying the applied voltage [71, 76]. After the formation of the AAO layer, it can be transferred and bonded with other substrates (e.g., Si wafers) [74, 77]. Then the catalyst (Au, Ag, Cu, etc.) nanoparticle array can be created on the substrate through the AAO layer. Figure 23 shows a typical evaporated Au nanoparticle array formed with the assistance of an AAO mask [77].

Upon obtaining the Au nanoparticle decorated substrate, the Si-NWs array can be grown based on the VLS mechanism. Figure 24 shows the Si-NWs array grown on the Si (111) substrate (shown in Fig. 23), with $SiCl_4$ as the precursor gas at 900°C. The resulting Si-NWs array follows the Au nanoparticle pattern, with good size control.

In addition, it is also noted that nano-imprint lithography is actively studied to pattern the catalyst metal layer and holds great potential to prepare large area Si-NWs arrays with low cost and high controllability [78]. Furthermore, the preparation of large-area and highly-ordered Si-NWs arrays embedded in polymer substrates has been successfully realized by transferring the VLS grown Si-NWs array, which paves the way for flexible Si-NWs-based solar cells [79].

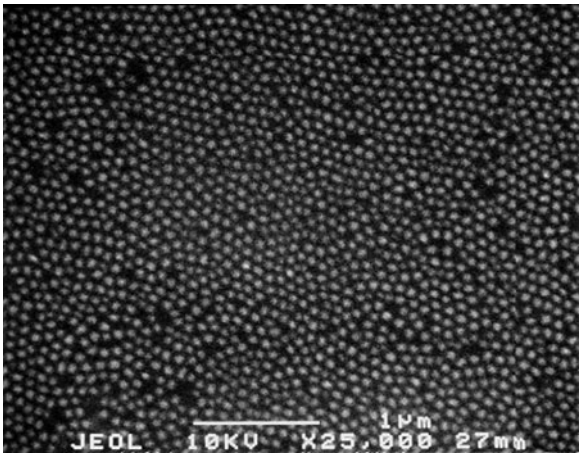

Fig. 23 Au nanoparticle array deposited through an AAO mask manufactured from an aluminum plate having multidomains. The average diameter, spacing and height of the nanoparticles are ~53, 100 and 5 nm, respectively. (Reprinted with permission from [77], copyright 2006, American Chemical Society)

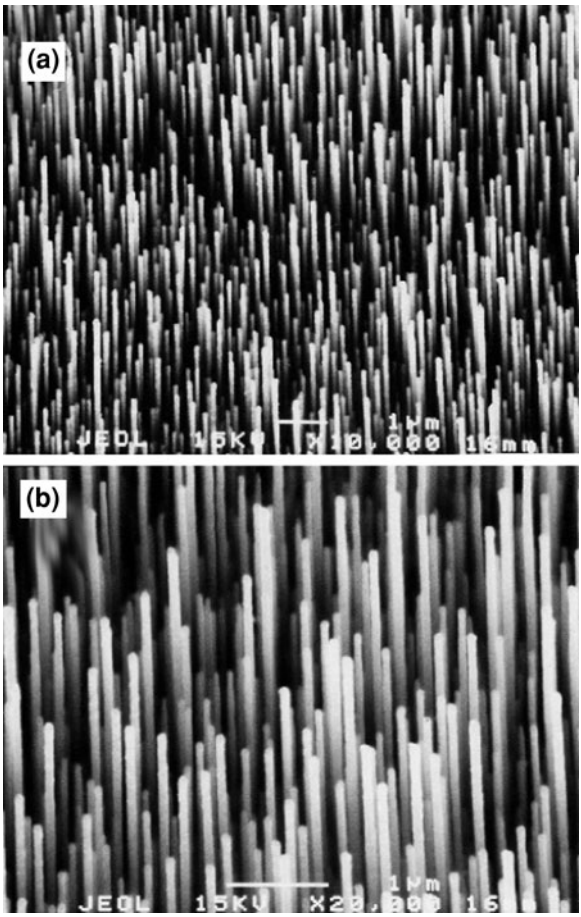

Fig. 24 Si-NW array with different magnifications grown on the substrate shown in Fig. 23. **a** Low magnification and **b** high magnification SEM images of vertically aligned, diameter-controlled Si-NWs grown from ordered Au dots on Si(111) substrates. The average diameter of the Si-NWs is ~72 nm. (Reprinted with permission from [77], copyright 2006, American Chemical Society)

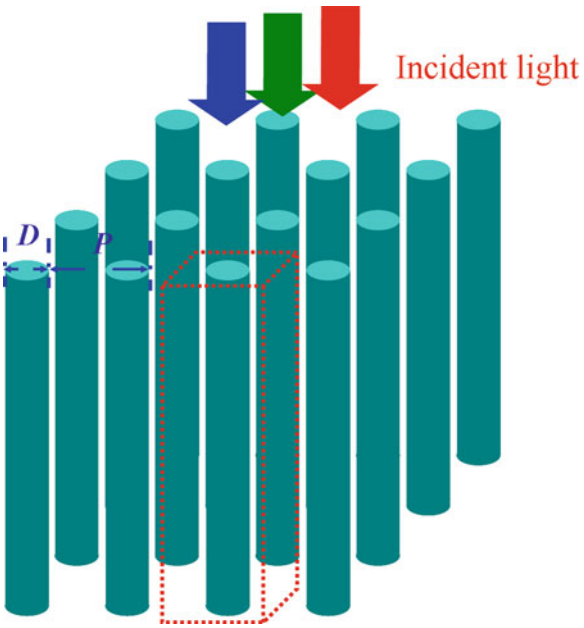

Fig. 25 Schematic of the stand-alone Si-NWs array studied by simulation. (Reprinted with permission from [87], copyright 2009, American Institute of Physics)

2.2.2 Optical and Electrical Characteristics of Stand-Alone Si-NWs Arrays

One of the most attractive advantages of using Si-NWs arrays in solar cells is the decoupling between light trapping and photogenerated carrier extraction [8]. In other words, Si-NWs can be grown long enough to effectively trap the incident photons and thin enough to efficiently collect the photogenerated carriers, enabling the utilization of low-grade raw materials, reducing the manufacturing cost. For either effective light absorption or efficient photogenerated carrier collection, the trade-off between the manufacturability (e.g., cost, controllability, reproducibility) and the resulting PCE should be considered. For instance, Si-NWs tend to break down if they are too thin or too long, which eventually leads to degraded photogenerated carrier extraction. Electrode contact and the light absorption capability would also be negatively impacted. These factors can explain why the present Si-NW-based solar cells have low PCEs, below 1% [80–82]. Therefore, providing the optimal microstructural parameters, such as array periodicity, Si-NWs diameter/length, is critical to the fabrication of Si-NWs-based solar cells.

Enhanced light absorption by Si-NWs arrays has been demonstrated empirically, especially in the high-energy regime of the solar spectrum [18, 50]. It was also observed that periodic and highly-ordered Si-NWs arrays are desirable for such a purpose [83]. Recently, the Chen group from Massachusetts Institute of Technology studied the optical characteristics, including light reflection, transmission and absorption, for a periodic stand-alone Si-NWs array (schematically shown in Fig. 25) with variable Si-NWs length/diameter at a fixed array periodicity of 100 nm using the transfer matrix method (TMM) [84]. Figure 26 shows

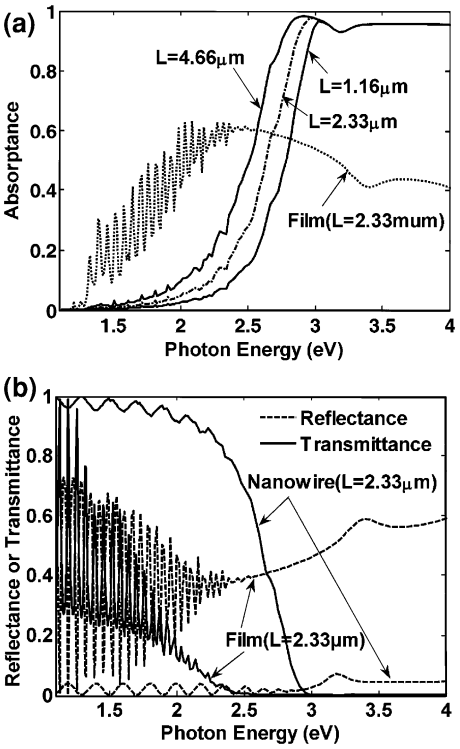

Fig. 26 **a** Absorption spectra of the Si-NW arrays as a function of the Si-NW length, and **b** reflection and transmission spectra of the 2330 nm long Si-NW array. The array periodicity and Si-NW diameter are fixed at 100 and 50 nm, respectively. The spectra of the 2330 nm thick Si film serve as the reference. (Reprinted with permission from [84], copyright 2007, American Chemical Society)

the optical characteristics of the Si-NWs array as a function of Si-NWs length. The diameter of the Si-NWs are fixed at 50 nm, and the incident light, parallel to the Si-NWs axes, varies from 1 to 4 eV, covering the majority of the solar spectrum [85]. It is clearly seen that the light absorption of a stand-alone Si-NWs array is above 95% in the high-energy regime (>2.8 eV) of the solar spectrum, much higher than that of the Si thin film counterpart. However, the light absorption of the Si-NWs array sharply decreases to nearly zero when the energy of the incident light is below $\sim$2.8 eV for an array of Si-NWs with lengths of 1160 nm. Even for the 4660 nm length Si-NW array, the light trapping capability is inferior to that of a 2330 nm thick Si film below the energy of $\sim$2.6 eV. As indicated in Fig. 26b, the poor light absorption for Si-NWs arrays in the low-energy region mainly stems from high light transmission in this energy regime. Low light reflection in the entire energy range, i.e., 1–4 eV, demonstrates the excellent antireflection function of Si-NWs arrays.

To evaluate the overall light trapping capability for solar cell applications, the ultimate efficiency (η) is calculated according to the following formula [30, 84, 86]:

$$\eta = \frac{\int_{E_g}^{\infty} \frac{E_g \times I(E) \times \alpha(E)}{E} \mathrm{d}E}{\int_0^{\infty} I(E) \mathrm{d}E}, \tag{5}$$

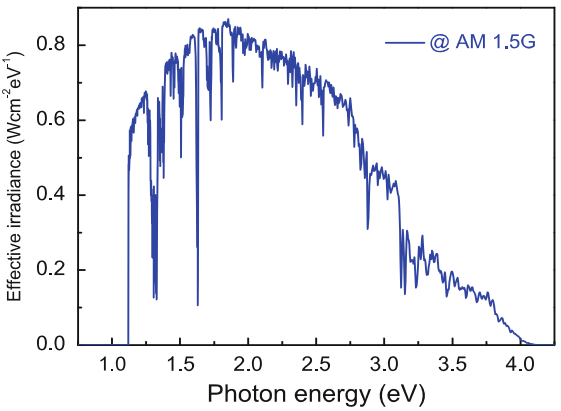

Fig. 27 Effective irradiance of the solar spectrum under AM 1.5G for single band gap Si solar cells. The effective irradiance is defined as the product of the irradiated power density and (E_g/hv)

where E_g is the band gap for the material ($\sim$1.12 eV for Si), E is the photon energy, $I(E)$ is the solar energy density spectrum, and $\alpha(E)$ is the absorption spectrum. From Eq. 5, one notes that η is defined as the optical–electrical conversion capability, provided that a photon with the energy above E_g, which can be trapped by the solar devices, is converted into one electron–hole pair with energy equal to E_g, and the electron–hole pair can be completely extracted for external output. In other words, when calculating the ultimate efficiency, the internal quantum efficiency is assumed to be 100%. The calculated η for the Si-NWs arrays with the lengths of 1160, 2330 and 4660 nm are $\sim$4.4, $\sim$5.8 and $\sim$7.8%, respectively. However, for the 2330 nm thick Si film, the ultimate efficiency reaches $\sim$15.5%, almost twice that of the best Si-NWs array. Thus, it is concluded that strong light absorption only in the high-energy regime of the solar spectrum does not make Si-NWs arrays competitive with Si thin films.

This can be understood from the potential contribution of the solar spectrum to a single junction solar cell. Figure 27 depicts the effective irradiance, or the product of the irradiated power (under AM 1.5G) per cm^2 and (E_g/hv) (note that for the photons with energy below E_g, this value is 0, i.e., no generation of electron–hole pairs), which illustrates the potential maximum power conversion capability. It is clearly shown that the effective irradiance for Si solar cells in the low-energy regime of the solar spectrum ($\sim$2 eV) plays a more profound role than in the high-energy regime to enhance the PCE. Due to the poor light absorption in the low-energy regime, it is reasonable that the ultimate efficiency for the 4660 nm Si-NW array is lower than that of the 2330 nm thick Si film. Similar to the case of increasing the Si-NWs' lengths (as demonstrated in Fig. 26a), increasing the Si-NWs diameters from 50 to 80 nm also leads to a redshift of the absorption edge [84]. However, the limited redshift still does not improve the overall light absorption of the Si-NWs array to be comparable to that of Si thin films with the same thickness. As discussed below, the poor light absorption for the Si-NWs

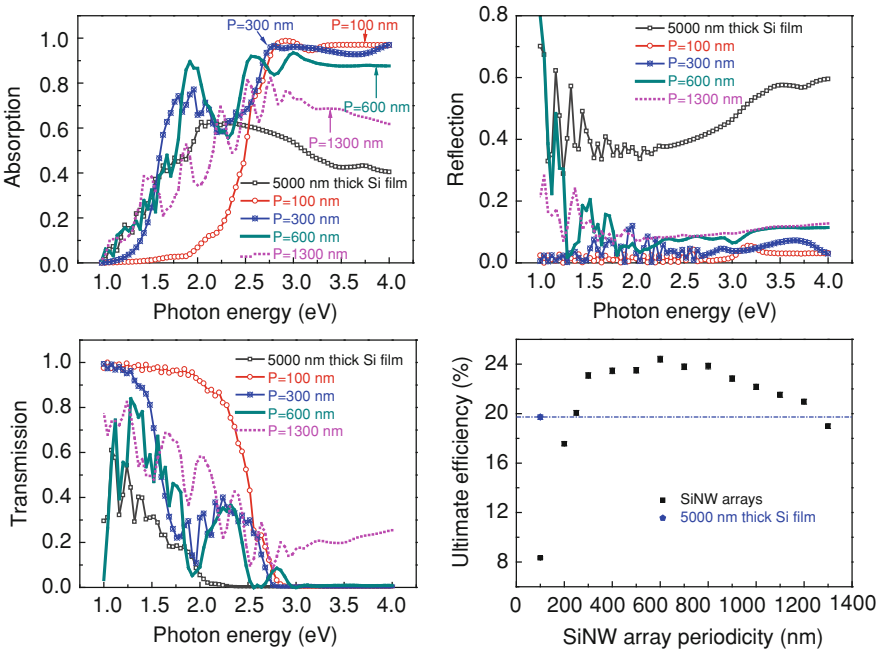

Fig. 28 **a** Absorption, **b** reflection, and **c** transmission spectra of the Si-NW arrays with different periodicities, *P*, of 100, 300, 600 and 1300 nm. The ultimate efficiency, η, of the Si-NW arrays as a function of *P* is summarized in **d**. The length of the Si-NWs in the array is 5000 nm, and the ratio of the Si-NW diameter to the array periodicity is fixed at 0.5. The 5000 nm thick Si film serves as a reference. (Reprinted with permission from [87], copyright 2009, American Institute of Physics)

arrays discussed by Chen et al. is due to their relatively small periodicity of 100 nm.

More recently, our group conducted a study on the impact of the Si-NWs array's periodicity to the optical characteristics using the finite element method (FEM) and presented the underlying physics responsible for the observations [87]. Figure 28a–c shows the light absorption, reflection and transmission spectra of the Si-NWs arrays as a function of periodicity. The Si-NWs length is set to 5000 nm, and the ratio of the Si-NWs diameter (*D*) to the array periodicity (*P*) is fixed at 0.5. One notes that the shift of the light absorption edge is much more sensitive to the array periodicity.

When the array periodicity is increased to 600 nm, the light absorption for the Si-NWs array is higher than that of the reference sample, i.e., the Si film with the same thickness of 5000 nm, almost in the entire energy range of 1–4 eV. As indicated by the transmission spectrum in Fig. 28c, the evident redshift of the light absorption edge can be attributed to the significantly suppressed light transmission in the lower energy region of the solar spectrum with an increased array periodicity. However, as the array periodicity is further increased, the

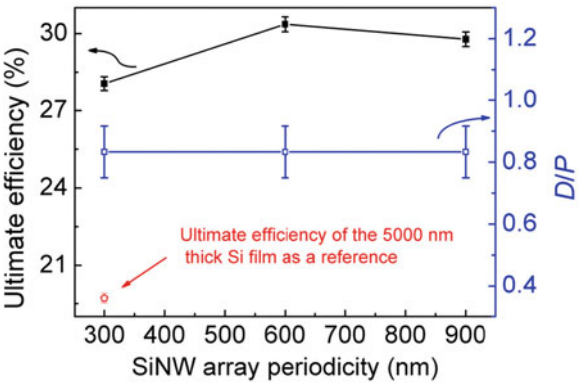

Fig. 29 Maximum ultimate efficiency and the corresponding *D*/*P* for the Si-NW arrays as a function of the array periodicity ranging from 300 to 900 nm. The value for the 5000 nm thick Si film is shown as a reference. (Reprinted with permission from [87], copyright 2009, American Institute of Physics)

spacing between neighboring Si-NWs also increases, resulting in increased light transmission, as indicated by the transmission spectrum of the Si-NWs array with a periodicity of 1300 nm. Moreover, light reflection (see Fig. 28b) is gradually enhanced due to the increased cross-sectional area of the Si-NWs. Accordingly, the light absorption is degraded when the array periodicity becomes too large. Figure 28d summarizes the calculated ultimate efficiencies, η. In agreement with the light absorption change with the array periodicity, η first increases significantly when increasing the array periodicity from 100 to 300 nm. Beginning with the Si-NWs array with the periodicity of 250 nm, η already becomes larger than that of the reference Si film with the same thickness of 5000 nm ($\sim$19.7%). As the array periodicity is further increased to 600 nm, η slightly increases to a maximum value of $\sim$24% due to the combined effects of the suppressed light transmission in the low-energy regime and the increased light reflection. The slight decrease in η can be ascribed to light transmission in the high-energy regime in addition to the increased light reflection when the array periodicity is above 600 nm.

Our further study reveals that the maximum ultimate efficiency for each periodicity ranging from 300 to 900 nm can be achieved when the ratio of the Si-NWs diameter to array periodicity (*D*/*P*) is around 0.8 [87]. At this *D*/*P* value, η of $\sim$30.5% is achievable for the Si-NWs array with the array periodicity of 600 nm, as demonstrated in Fig. 29. More meaningfully, the window of the array periodicity and *D*/*P* is wide enough to realize a higher light trapping capability compared to the Si film counterpart, which gives the manufacturing side more process to choose from. It is interesting to note that the Lewis and Atwater group from California Institute of Technology has recently reported the synthesis of Si-NWs with 10 μm minority carrier diffusion lengths by Cu-catalyzed VLS growth [88]. Accordingly, it is believed that the resulting high PCE of the Si-NWs array-based on an optimized optical design is achievable.

Kayes et al. have explored the carrier transport properties of stand-alone Si-NWs via simulation and discussed the relationship between the illuminated *I*–*V* characteristics and geometrical parameters, such as the length and diameter, and the defect state densities in the quasi-neutral and depletion regions [8]. In their

study, it is assumed that the carrier transport is along the radial direction for the radial p–n junction configuration. It is found that for a given Si-NWs length, the short circuit current density, J_{sc}, is almost independent of the minority carrier diffusion length if the minority carrier diffusion length is larger than the Si-NWs radius. However, the J_{sc} in the solar cells with the conventional planar p–n junction configuration significantly decreases with the minority carrier diffusion length. For the radial junction case, different from J_{sc}, V_{oc} shows dependence on the Si-NWs' length, and decreases with an increase in the Si-NWs' length. This can be attributed to the increased junction area, and thus a decreased shunt resistance. Under the illuminated condition of the AM 1.5 spectrum, it is also reported that the Si-NWs-based solar cell can reach a PCE of $\sim$11%. The Si-NWs have diameters of 100 nm and lengths between 20 and 500 μm, the minority-electron diffusion length is 100 nm (comparable to the Si-NWs diameters), and the recombination center densities of 7×10^{18} cm^{-3} in the quasi-neutral region and 10^{14} cm^{-3} in the depletion region. However, for the Si wafer counterpart with the same material parameters, the PCE is only $\sim$1.5% and saturates when the thickness is over 450 nm. This study points out the great potential of stand-alone Si-NWs-based solar cells. Here it is noted that the above study does not account for any interaction between the incident light and the studied Si-NWs array (and hence the enhanced light absorption). After considering the enhanced light absorption for the optically optimized Si-NWs array, the PCEs of Si-NWs-based solar cells should become much more competitive with that of planar Si solar cells.

2.2.3 Research Status of Stand-Alone Si-NWs-Based Solar Cells

In 2007, the Lewis and Atwater group demonstrated a Si-NWs array-based photoelectrochemical cell [89]. The highly-ordered and vertically-aligned n-type (resistivity of $\sim$0.32 Ω cm) Si-NWs array (see Fig. 30) with wires of diameter of $\sim$2 μm, length of $\sim$20 μm, and an array periodicity of $\sim$7 μm was grown on a degenerately doped n-type Si (111) wafer via VLS growth. The Si-NWs array is immersed into a 1,1′ dimethylferrocene $(Me_2Fc)^{+/0}$ redox system in CH_3OH to form the p–n junction. This method can easily realize uniform coverage of the transparent electrode over the Si-NWs surface. The measured V_{oc} and J_{sc} of the Si-NWs array-based solar cell under AM 1.5G are 389 ± 18 mV and 1.43 ± 0.14 mA/cm^2, which is much better than that of the control sample without the Si-NWs array (V_{oc} : 232 ± 8 mV; J_{sc} : 0.28 ± 0.01 mA/cm^2).

Also in 2007, Tsakalakos et al. of General Electric's Global Research Center, USA fabricated the first Si-NWs-based all-inorganic solar cell [80]. Figure 31a, b shows the schematics of the Si-NWs-based solar cell configuration and the SEM images of the Si-NWs under different views (the cross-sectional view in the top-left). The p-type (estimated doping concentration of $\sim 10^{18}$ cm^{-3}) Si-NWs with diameters of 109 ± 30 nm and length of $\sim$16 μm were grown without orientation on a stainless steel foil coated by 100 nm thick Ti_2N using the Au catalyzed VLS growth (the precursor gas is the mixture of SiH_4, H_2, HCl and $B(CH_3)_3$). Here the

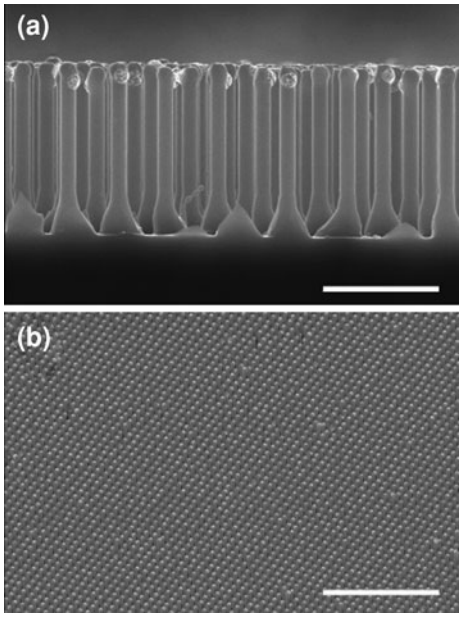

Fig. 30 **a** Cross-sectional (scale bar: 15 μm), and **b** 45° view (scale bar: 85.7 μm) SEM images of an Si wire array prepared by the VLS growth combined with the prepatterned Au catalyst. (Reprinted with permission from [89], copyright 2007, American Chemical Society)

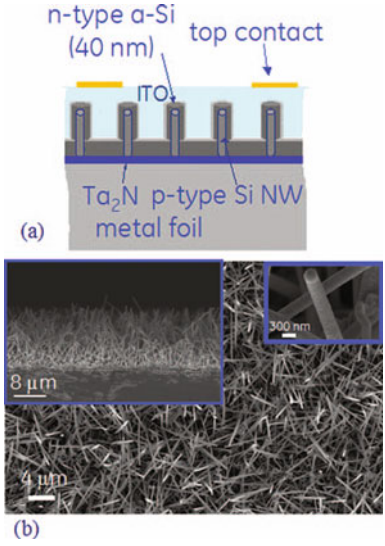

Fig. 31 **a** Schematic of the Si-NW-based all-inorganic solar cell using a stainless steel foil as the substrate, and **b** the SEM images of the Si-NWs under different views. (Reprinted with permission from [80], copyright 2007, American Institute of Physics)

Ti_2N film serves as the back electrode and also prevents interdiffusion between the Si and the steel substrate. As indicated by the SEM images in Fig. 31b, the synthesized Si-NWs randomly distribute on the substrate owing to the unpatterned Au catalyst. The p–n junction is introduced through depositing the 40 nm thick n-type a-Si:H layer by PECVD. This is followed by the ITO layer deposition with

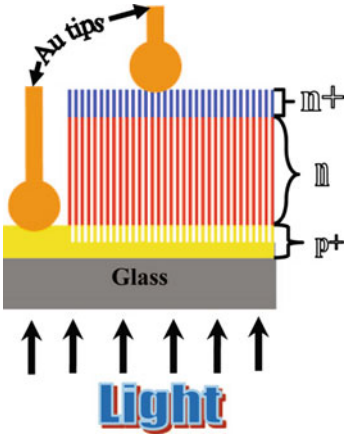

Fig. 32 Schematic of the Si-NW-based solar cell prepared by the electroless etching of the corresponding μc-Si (n^+)/μc-Si (n)/μc-Si (p^+) structure on glass. (Reprinted with permission from [90], copyright 2009, American Chemical Society)

the thickness of ~200 nm to electrically connect the Si-NWs. Then the top finger electrode consisting of 50 nm thick Ti and 2000 nm thick Al is prepared by shadow evaporation. The PCE of the fabricated solar cells with the size of 1×1 cm^2 was measured at only ~0.1% under AM 1.5G although the enhanced light absorption is obvious. The low PCE can be ascribed to the poor photogenerated carrier separation capability and poor electrical contact, both related to the randomly grown Si-NWs array.

Except for the VLS grown Si-NWs array, the low-cost "top-down" approaches also attract a lot of attention to fabricate stand-alone Si-NWs-based solar cells. Sivakov et al. fabricated Si-NWs-based solar cells by etching the corresponding $\mu c - \mathrm{Si}\ (n^+)/\mu c - \mathrm{Si}\ (n)/\mu c - \mathrm{Si}\ (p^+)$ structure on glass substrates using the electroless chemical etching solution prepared by mixing 0.02 M $AgNO_3$ and 5 M HF with a volume ratio of 1:1 [90]. Figure 32 shows the schematic of the cell structure with a superstrate configuration [91]. The $\mu c - \mathrm{Si}\ (n^+)$, $\mu c - \mathrm{Si}\ (n)$ and $\mu c - \mathrm{Si}\ (p^+)$ layers with the respective thicknesses of 300, 2000, and 200–400 nm were prepared by electron beam evaporation and the laser annealing, with respective doping concentrations of 5×10^{19}, 6×10^{16}, and 5×10^{19} cm^{-3}. As indicated by the cross-sectional SEM image shown in Fig. 33a, the resulting Si-NWs are vertically aligned on the glass substrate. The length and diameter of the Si-NWs vary from 2300 to 2500 nm, and from 20 to 100 nm respectively, as estimated from the SEM and TEM measurements. Figure 33b shows the measured optical characteristics, indicating excellent light trapping capability, especially in the high-energy regime of the solar spectrum compared to the Si thin film counterpart. The *I–V* characteristics of these solar cells are recorded by contacting the Au tips with the radius of 450 μm onto the Si-NWs top surface and the p^+ Si-film layer (see Fig. 32). The V_{oc} is recorded in the range of 410–450 mV and the J_{sc} varies from 13.4 to 40.3 mA/cm^2 when measuring different points on the same sample. Despite the error in calculating the Au tip area (hence the J_{sc}), the PCE of the cell is in the range of 1.7–4.4%. Further enhancement of the PCE can be

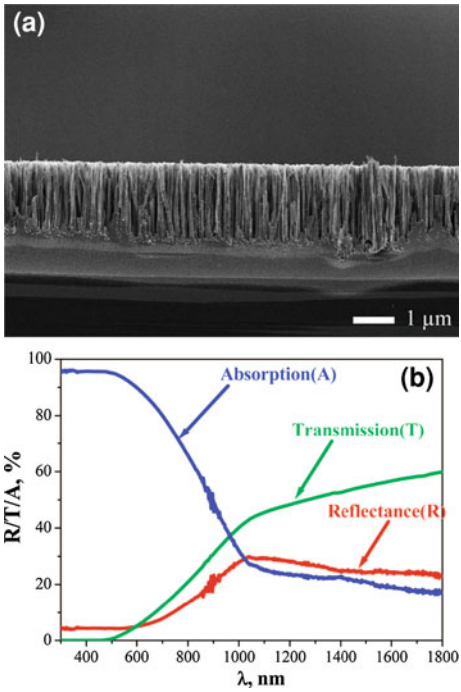

Fig. 33 **a** Cross-sectional SEM image of vertically aligned Si-NWs on glass after electroless etching, and **b** the optical characteristics of the above Si-NW array. (Reprinted with permission from [90], copyright 2009, American Chemical Society)

expected by optimizing the Si-NWs' structural parameters, such as diameter, array periodicity, and the electrode configuration.

More recently, the Yang group at the University of California at Berkeley reported Si-NWs-based solar cells with the controllable Si-NWs diameters and array periodicity using the RIE-based "top-down" technique combined with a self-assembled SiO_2 monolayer mask [92]. In their study, to mimic the PV response of the stand-alone Si-NWs layer, a highly doped Si wafer was used as the substrate to minimize the PV contribution from the substrate and an epitaxial Si thin layer on the wafer is employed to manufacture the Si-NWs array. After the formation of the Si-NWs array, boron diffusion was performed to form radial p–n junctions, followed by finger metal electrode deposition. Figures 34a, b respectively show the SEM image of the resulting Si-NWs array (Si-NWs with diameters of $\sim$390 nm, lengths of $\sim$5 μm, and an array periodicity of $\sim$530 nm), and the optical image of the large-scale Si-NWs-based solar cells on the same substrate after isolation. The illuminated *I–V* characteristics recorded under AM 1.5G demonstrate a PCE of $\sim$4.83% (V_{oc}: 525 $\pm$ 2 mV; J_{sc}: 16.45 $\pm$ 0.19 mA/cm^2; FF: 0.559 $\pm$ 0.002) for the solar cell with the absorber consisting of the above Si-NWs array and a 3 μm thick underlying Si layer, which is $\sim$20% higher than that of the Si ribbon solar cell with the same total thickness, i.e., 8 μm [93]. Here it should be noted that the electrode configuration is yet to be optimized for Si-NWs-based solar cells. They further declare that the

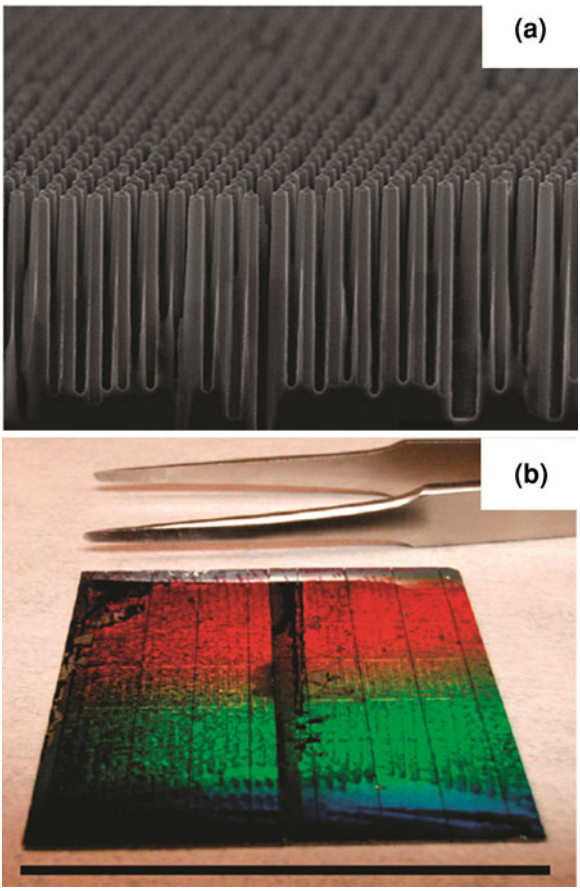

Fig. 34 **a** Titled SEM image of the Si-NWs array after forming the radial p–n junction (the scale bar: 1 μm), and **b** the tilted optical image of the Si-NW array-based solar cells on the same substrate after isolation (the scale bar: 4 cm). (Reprinted with permission from [92], copyright 2010, American Chemical Society)

light absorption mainly occurs in the Si-NWs array, and an optical path length enhancement factor of ~73 can be achieved, which is much larger than the randomized scattering limit (~25 without a back reflector) [94].

Despite the great potential held by Si-NWs-based solar cells, the currently reported PCE record from the literature is still relatively low compared to mainstream Si wafer cells. To further improve the PCE of stand-alone Si-NWs-based solar cells, the following points need to be addressed:

(i) *Structural optimization of the Si-NWs*. Si-NWs-based solar cells make it possible to design the light trapping and photogenerated carrier collection processes due to the decoupling between them. However, for practical operation, the trade-off between light trapping and carrier collection should be considered when designing high-efficiency devices. For example, the surface defect states are critical, especially for Si-NWs prepared by the etching approaches [50] because they lead to a decreased V_{oc} [8]. How to

achieve compromise between the enhanced light absorption and the degraded V_{oc} while increasing the Si-NWs' lengths needs to be investigated via simulations coupling both optical and electrical aspects.

(ii) *Optimized top transparent electrodes*. Optimal electrode configuration is another key factor to realizing high-efficiency solar cells. Especially for Si-NWs-based solar cells, high contact resistance needs to be addressed through optimization of nanoscale design and manufacturing processes. The conformal deposition of the top transparent electrode to uniformly cover the Si-NW surface is necessary to effectively extract the photogenerated carriers.

(iii) *Reducing the surface defect density*. Although the radial p–n junction based solar cells allow for the usage of low-grade materials with high bulk defect densities, the defect state density on Si-NWs surfaces needs to be minimized. Surface defects can trap photogenerated carriers, act as recombination zones and degrade the solar performance [95, 96]. Therefore effectively reducing the number of Si-NWs surface defect density remains important to obtaining high efficiency.

2.3 Si Thin Film Solar Cells Textured with Si Nanostructures

In this section, surface texturing of Si thin film solar cells using three types of Si nanostructures, including Si-NWs (or Si nanopillars (Si-NPs)), Si nanocones (Si-NCs), and Si nanoholes (Si-NHs), are discussed for efficiency boosting. The preparation of Si-NWs arrays was introduced in Sect. 2.2.1. Therefore, the fabrication techniques of the Si-NCs and Si-NHs-textured surfaces are to be discussed in detail in this section.

2.3.1 Preparation of Si Thin Films Textured with Nanaostructures (Si-NCs and Si-NHs)

Different from the "bottom-up" paradigm in preparing stand-alone Si-NWs on foreign substrates, the fabrication of the Si nanostructure-textured Si thin films is mainly based on "top-down" processes, which are able to meet the solar cells manufacturing requirements, i.e., low cost, large scale, and high throughput. Several representative methods used for the preparation of Si-NC- and Si-NH-textured surfaces will be discussed. Hsu et al. prepared highly-ordered Si-NC-textured surfaces using C_2ClF_5/SF_6-based isotropic RIE on the corresponding Si-NWs arrays, which were formed by the Cl_2-based anisotropic RIE of Si wafers combined with a monolayer of SiO_2 nanospheres as a Langmuir–Blodgett mask (for more details, refer to Sect. 2.2.1) [19]. Figure 35 illustrates the fabrication process and the corresponding SEM images. In this method, the Si-NCs' structural parameters, such as height, base diameter, and array periodicity can be controlled

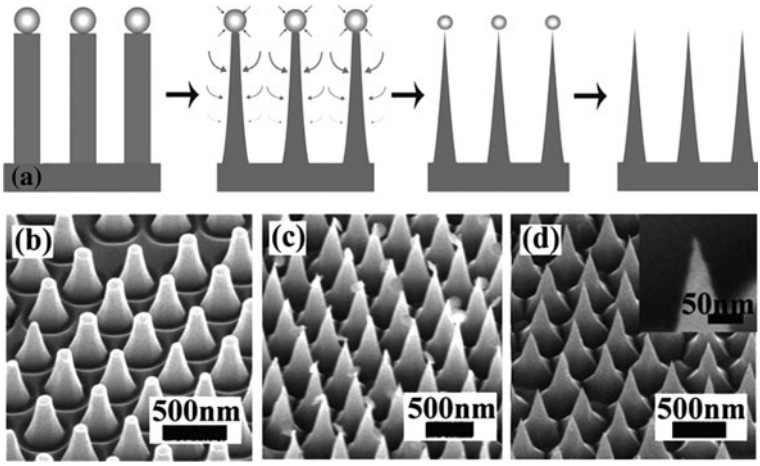

Fig. 35 **a** Schematic of the fabrication process of a highly-ordered Si-NC-textured surface, **b–d** show the SEM images corresponding to the intermediate and final steps. (Reprinted with permission from [19], copyright 2008, American Institute of Physics)

during the preparation of the Si-NWs array. It is interesting to note that this method has been successfully applied to fabricate Si-NC-textured a-Si:H films, paving the way for its application in Si thin film-based solar cells [9].

Another approach to make Si-NC-textured surfaces is reported based on one-step self-assembly processes without involving the mask preparation [20, 97–99]. Figure 36 schematically shows the process flow using the "self-masking method" [20]. During the process, a plasma with precursor gases of SiH_4, CH_4, Ar, and H_2 can generate and deposit SiC nanoparticles on the substrate surface as demonstrated in Fig. 36a, b. This is followed by the introduction of Ar and H_2 plasma to etch the Si substrate and obtain the Si-NC array using the SiC nanoparticles as the hard mask. It is expected that Si-NC arrays can be made in large scales using this method. Figure 37a, b shows the as-prepared Si-NC texturing on single-crystal and polycrystalline Si substrates, respectively. It is noted that during the processes, the substrate temperature was maintained below 250°C, which facilitates the usage of low-temperature and low-cost substrates. In Fig. 37a, a Si-NC density of $\sim 1.5 \times 10^{11}/cm^2$ and aspect ratio of 50 are shown. For this approach, the structural parameters of the Si-NC array, such as the Si-NCs' base diameter, spacing, and height can be adjusted through varying the size and density of the SiC nanoparticles via modifying the plasma conditions, and the substrate temperature.

Analogous to macrohole-textured surfaces in Si wafer-based solar cells, the excellent antireflection property of the Si nanoholes array-decorated surfaces makes Si-NHs promising in Si thin film-based solar cells. For the sake of cost reduction, only the fabrication approaches based on cost-effective mask or maskless processes are discussed here. Li et al. developed the laser nanoimprinting technique to create large area Si-NH-textured surfaces [100]. After coating the

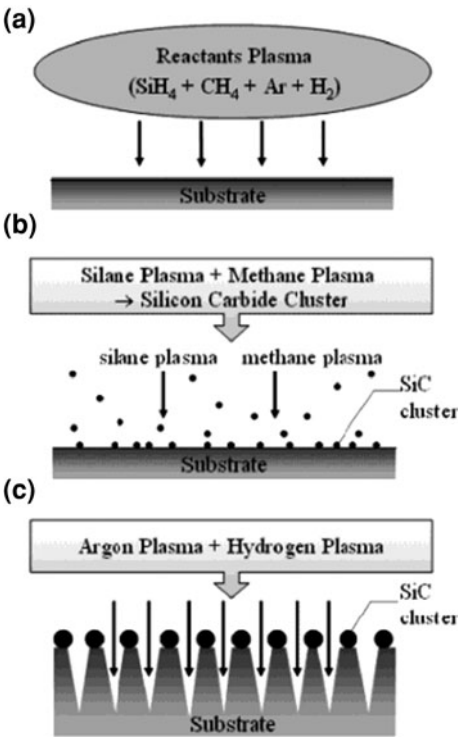

Fig. 36 Schematic of the procedure for preparing the Si-NC-textured surface using the one-step self-assembly method. **a** The reactive gases are composed of silane, methane, argon, and hydrogen; **b** the SiC nanosized clusters are formed from the reaction of SiH_4 and CH_4 plasma and uniformly distributed on the substrate surface; and **c** the unmasked region is etched by Ar and H_2 plasma, whereas the region masked by SiC caps protects the substrate from etching, and hence creates the conical tips. (Reprinted with permission from [20], copyright 2004, American Chemical Society)

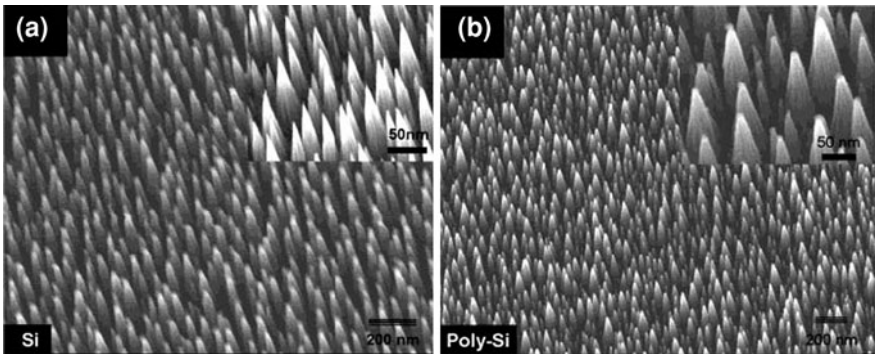

Fig. 37 Tilted SEM images of the Si-NC array on **a** single-crystal and **b** polycrystalline Si substrates using the one-step self-assembling method depicted in Fig. 36. (Reprinted with permission from [20], copyright 2004, American Chemical Society)

sample with a monolayer of self-assembled SiO_2 nanospheres, a focused laser beam is directed onto the SiO_2 nanospheres. Due to the extremely high temperature at the contact point between the SiO_2 and substrate, which results from the optical resonance and near-field effects [101], the substrate in the vicinity of the

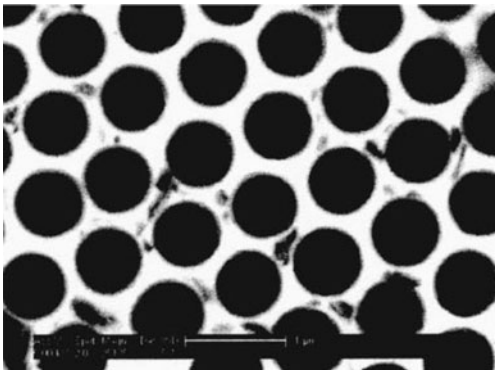

Fig. 38 SEM image of Si-NH-textured Si (100) wafer prepared by the laser nanoimprinting technique combined with the self-assembled SiO_2 nanosphere monolayer (the scale bar is 1 μm). The average diameter of the SiO_2 nanospheres is 970 nm, and the fluence of the single laser pulse (KrF, wavelength: 248 nm) is 1 J/cm^2. (Reprinted with permission from [100], copyright 2004, American Institute of Physics)

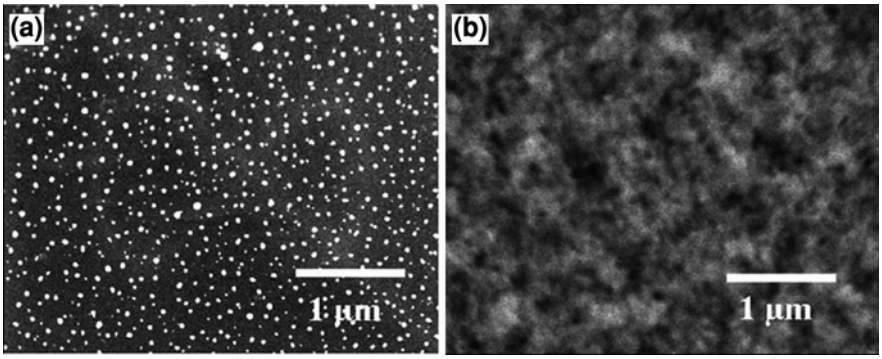

Fig. 39 SEM images of **a** the Ag nanoparticles on the Si wafer surface, and **b** the SiNHs array decorated surface after wet etching in the HF/H_2O_2 solution. (Reprinted from Tsujino et al. [102], copyright 2006, with permission from Elsevier)

nanospheres melts, forming hemisphere-shaped holes into the substrate. Figure 38 shows the SEM image of the Si-NH-textured Si (100) wafer prepared using SiO_2 nanospheres with diameters of ~970 nm with the fluence of a single laser pulse (KrF, wavelength: 248 nm) set at 1 J/cm^2. The Si-NH size and depth can be modulated by modifying the SiO_2 nanosphere size and the laser fluence. This method is applicable to Si thin films on glass and plastic substrates due to the localization of the melting.

Next, the randomly distributed Si-NH-textured surface is discussed, which can be prepared in a low cost and high throughput manner. The formation of the Si-NHs can be realized in the HF/H_2O_2 solution with the catalysis of noble metals such as Ag, Au, etc (see Sect. 2.2.1). Figure 39 shows the SEM images of (a) the

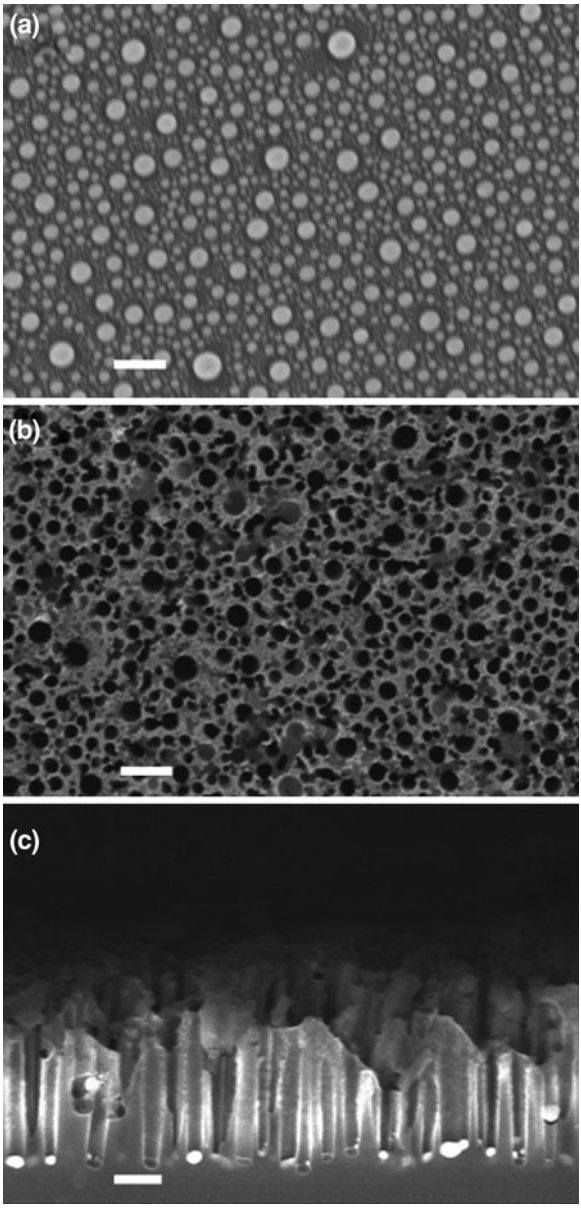

Fig. 40 SEM images of **a** the Ag nanoparticles on the Si wafer surface prepared by laser annealing of the Ag film, **b** the top and **c** cross-sectional views of the resulting Si-NH array after wet etching in the HF/H_2O_2 solution. In **c**, the white particles at the bottom of the Si-NHs are the residual Ag nanoparticles. The scale bar in the pictures is 200 nm

Ag nanoparticles on the multicrystalline Si wafer surface, and (b) the resulting randomly distributed Si-NH-textured surface after the wet etching in a mixture of 10% HF and 30% H_2O_2 (10:1 v/v) for $\sim$5 min [102]. The Ag nanoparticles are prepared using the electroless plating [103]. The dimensions of the Si-NHs are consistent with the Ag nanoparticles sizes and can be modulated by varying the Ag

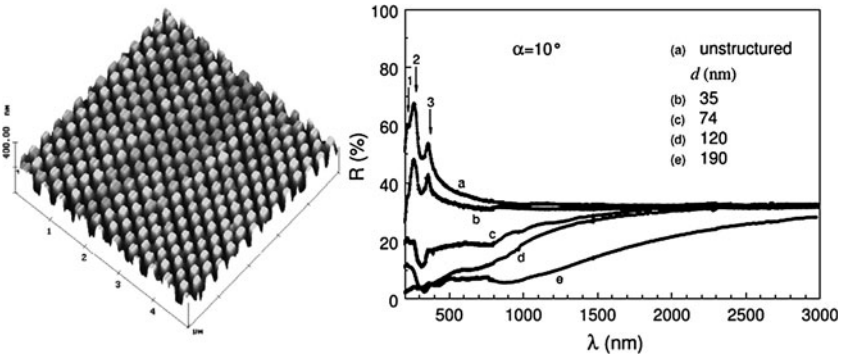

Fig. 41 AFM image of the Si-NW-textured surface (array periodicity: 300 nm) (*left*), and the reflectivity, *R* (*right*) of the Si-NW-textured surface with the same array periodicity of 300 nm and varying Si-NW array depths, *d*. The measurements were performed using unpolarized light at the incident angle of 10°. (Reprinted with permission from [64], copyright 2000, Institute of Physics)

nanoparticles size and distribution. The Si-NHs' depth can also be easily controlled by the etching time.

Our group has also developed a method to form the Ag nanoparticles by employing rapid laser annealing on an as-deposited Ag thin film [104]. The SEM image, as shown in Fig. 40a demonstrates that the Ag nanoparticles can be synthesized with a high density. Figure 40b, c shows the top and cross-sectional views of the etched Si surface using the HF/H_2O_2 mixture. It is clear that the resulting Si-NH array strictly follows the Ag nanoparticles pattern, which can be modified by the thickness of the Ag film, laser pulse energy, etc. Similar to the laser nanoimprinting technique, this approach is also applicable to Si thin films on glass or plastic due to the localized thermal effect of the laser annealing process.

2.3.2 Optical and Electrical Characteristics of Si Nanostructure-Textured Si Thin Films

It is well documented that the key advantage of the Si nanostructure texturing in thin film-based solar cells is its excellent antireflection property. It is thus expected that thicker texturing layers with large aspect ratios will lead to more efficient antireflection, as indicated in Fig. 41 [64]. However for solar cell applications, as discussed previously, other aspects must also be considered. The effective extraction of photogenerated carriers relies on optimized electrical contacts, which further depend on the conformal deposition of the electrodes on the Si nanostructure. Therefore, the thickness of the Si nanostructure layers is a compromise, also partially owing to the manufacturing concerns.

Different from the light multireflection mechanism based on geometrical optics in microscale surface textures for light absorption enhancement, the interaction

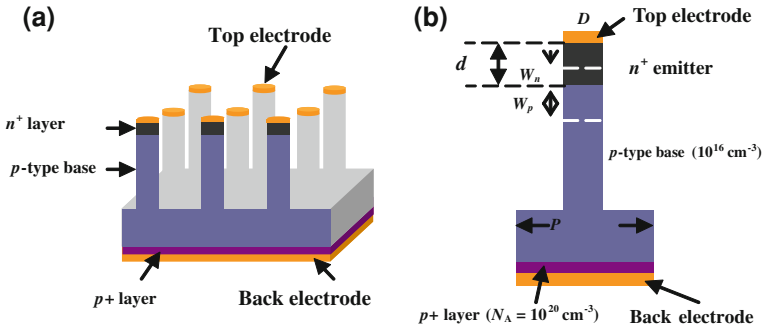

Fig. 42 **a** Schematic of the Si-NW-textured thin film-based solar cell, and **b** the unit used for the calculation of the optical and electrical characteristics

between the incident light and nanoscale surface textures follows elemental optical processes based on wave optics, such as scattering [30]. Enhanced scattering will significantly elongate the optical path length, hence increasing the light trapping capability, i.e., increasing the light absorption. Our group has systematically studied the optical characteristics of Si nanostructure-textured Si thin films, including Si-NWs, Si-NCs and Si-NHs [30, 31, 105, 106]. The results indicate that there is a critical value for the thickness of all the Si nanostructure textures. When the thickness is beyond this value, the light trapping capability becomes nearly saturated. From calculations, the optimized critical thicknesses for Si-NWs, Si-NCs and Si-NHs are $\sim$1000, 400, and 2000 nm, respectively. Furthermore, light absorption is strongly affected by array periodicity. Figure 42 schematically shows the Si thin film-based solar cell configuration with a Si-NWs-textured surface. During the calculation, the thickness of the Si thin film was fixed at 800 nm. The optically optimized Si-NWs length was set as 1000 nm, which is also acceptable for the high-quality electrode preparation. The ratio of the Si-NWs diameter (D) to P of 0.5 was taken from our previous studies [30, 31].

Figure 43a, c shows the light absorption, reflection, and transmission spectra of the studied structure (see Fig. 42a) with different Si-NWs array periodicities. As expected, the light absorption is significantly enhanced when incorporating the Si-NWs array into the device. More interestingly, the sample with a P of 100 nm shows a consistent absorption with the 800 nm thick Si film, and the absorption becomes stronger when the energy is above $\sim$2.2 eV. In the low-energy region of the solar spectrum, the wavelength of the incident light is much longer than the P of the Si-NWs array. Accordingly, incident light can easily penetrate through the Si-NWs array and reach the underlying Si layer. This statement is further evidenced by the reflection and transmission spectra for both samples in the corresponding energy region (see Fig. 43b, c). It was also observed that the "deviation" point of the absorption spectra for the Si film with and without Si-NWs array shifts towards the low-energy regime with increasing P. The deviation point for the sample with P of 200 nm is around 1.5 eV.

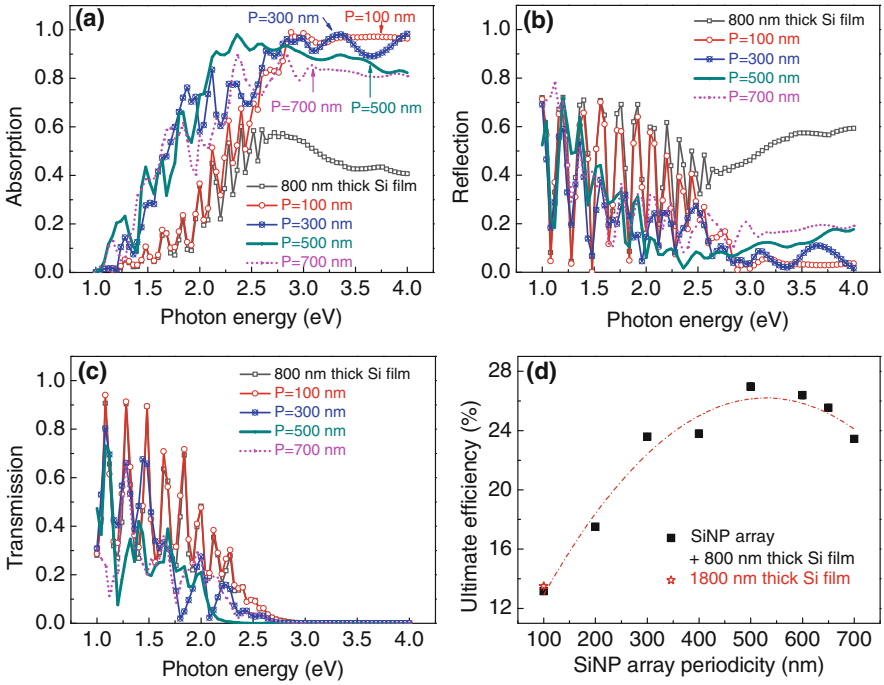

Fig. 43 **a** Absorption, **b** reflection, and **c** transmission spectra of the Si-NW (*length*: 1000 nm) textured Si *thin* films (thickness: 800 nm) as a function of the array periodicity, *P*. The ultimate efficiency is summarized in **d**. *D*/*P* is held constant at 0.5. The 800 and 1800 nm *thick* Si films serve as the reference. (Reprinted with permission from [30], copyright 2009, American Institute of Physics)

In the high-energy regime, the wavelength of the incident light is comparable with *P*. Thus, the scattering of the incident light is significantly enhanced, resulting in an elongated optical path and, therefore, enhanced light absorption, which is verified by the excellent light absorption of ~95% in the energy region above ~2.9 eV for the sample with *P* of 100 nm. As *P* increases, the incident light scattered by the structure shifts toward longer wavelengths and the reflection in the short wavelength range increases accordingly. As shown in Fig. 43a, the absorption peak shifts to ~2.5 eV with increasing *P* from 100 to 500 nm. On the other hand, decreased light absorption in the high-energy region was observed. However, the energy density is relatively weak in this regime of the solar spectrum and the decreased light absorption in this energy region is effectively compensated by the shift of the absorption edge. Further increasing *P* to 700 nm, the light reflection becomes so strong in the broad range that it cannot be compensated by the absorption edge shift, resulting in lower light absorption. Figure 43d shows the ultimate efficiency as a function of *P*, and the 1800 nm film serves as the reference. For the 800 nm thick Si film with the Si-NWs-decorated surface, the ultimate

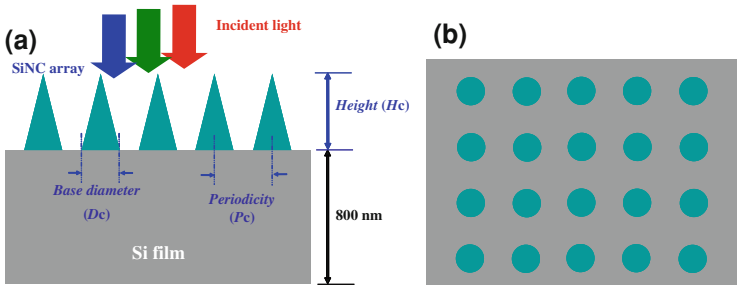

Fig. 44 Schematic of the **a** cross-sectional and **b** plane views of the Si-NC-textured thin film

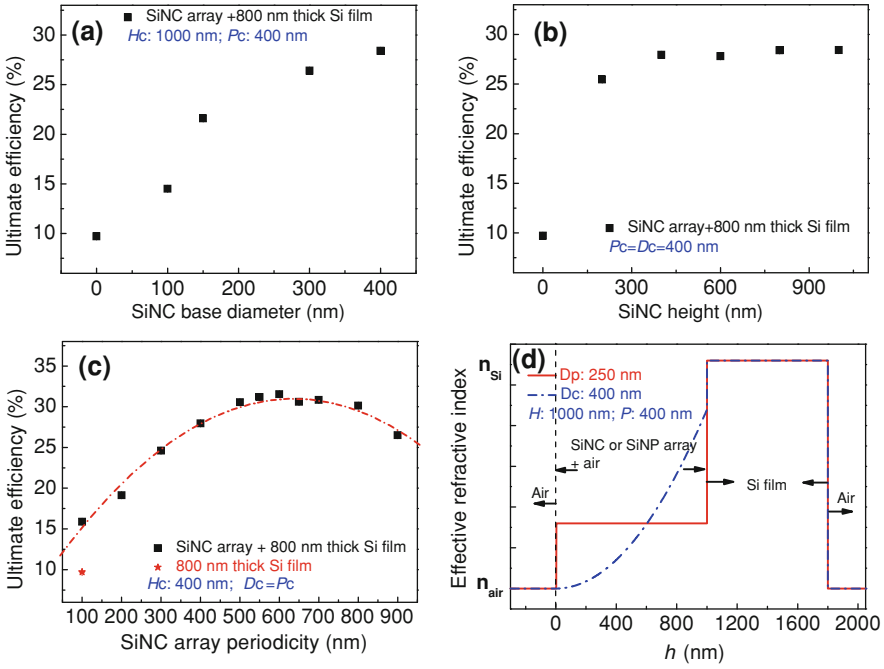

Fig. 45 Ultimate efficiency of the Si-NC-textured thin film as a function of **a** base diameter, D_c, **b** Si-NC height, H_c, and **c** array periodicity, P_c. **d** shows a comparison of the spatial distribution of the effective refractive indices for the Si-NC- and Si-NW-textured thin films

efficiency first increases with P, reaching a maximum of ~27% when P is ~500 nm, more than 200% of that of the 1800 nm thick Si film.

Following a similar methodology, the optical characteristics of the Si-NC- and Si-NH-textured thin films are also investigated using the FEM method [31]. Figure 44 shows the schematic of cross-sectional and top views of a Si thin film (800 nm) textured by a Si-NC array. This study indicates that for effective anti-reflection, the base diameter, D_c, of the Si-NCs should be equal to the array

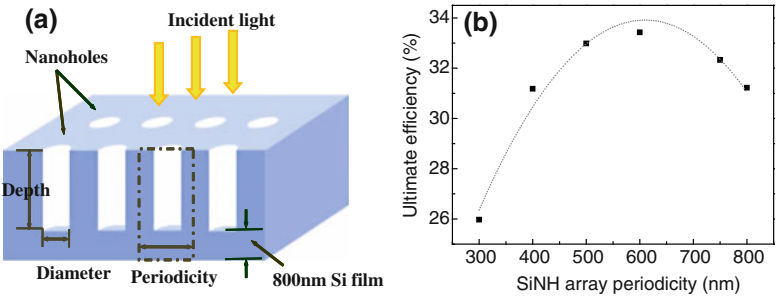

Fig. 46 **a** Schematic of the Si-NH structure for computational simulations, and **b** ultimate efficiency of the structure as a function of the array periodicity

periodicity, P_c, due to the more continuous spatial distribution of the effective refractive index between air and the underlying Si thin film, which is reflected by the continuously increasing ultimate efficiency with D_c (see Fig. 45a). As demonstrated in Fig. 45b, the ultimate efficiency becomes nearly saturated when the Si-NC height exceeds 400 nm. Further, it is believed that the conformal deposition of the top transparent electrode is realizable for this Si-NC height. The variation of the ultimate efficiency with P_c demonstrates a similar trend compared with the Si-NWs case, and a maximum value of $\sim$31.5% occurs at a P_c of 600 nm, although the total thickness is only 1200 nm (400 nm Si-NC + 800 nm Si thin film layer), as shown in Fig. 45c. This is much greater than the value of $\sim$27% for the optimized Si-NWs-textured Si thin film with a total thickness of 1800 nm, due to the continuous effective refractive index between air and the underlying Si layer (see Fig. 45d), enabling more efficient reduction of the incident light reflection, as suggested by the Fresnel theory [25].

For the Si-NH-textured surface (schematically shown in Fig. 46a), based on the similar mechanism of wave optics, it was found that the solar energy absorption could be optimized when the dimensions of the Si-NH array are set as follows: array periodicity of $\sim$600 nm (Fig. 46b), depth of 2000 nm, and the ratio of the Si-NH diameter to array periodicity of $\sim$87.5%.

Following the optical study, the electrical behaviors in the Si nanostructure-textured thin film-based solar cells are discussed in terms of the minority carrier diffusion length, doping concentration, and junction depth. The discussion is based on the optically optimized Si-NWs-textured (length: 1000 nm; P: 500 nm; D: 250 nm) Si thin film (thickness: 800 nm) [107]. In Sect. 2.2.2, the carrier transport in Si-NWs-based solar cells was briefly discussed for a radial p–n junction. Here, for the convenience of comparison with the Si thin film solar cells, the traditional planar p–n junction configuration is under consideration, as shown in Fig. 42. The p-type base has a light doping of 10^{16} cm^{-3}. A thin p^+ layer of 50 nm with the doping concentration of 10^{20} cm^{-3} is used to form a high-quality Ohmic contact with the back electrode. During the calculation, Shockly-Reed-Hall and Auger recombinations are considered in the lightly- and heavily-doped

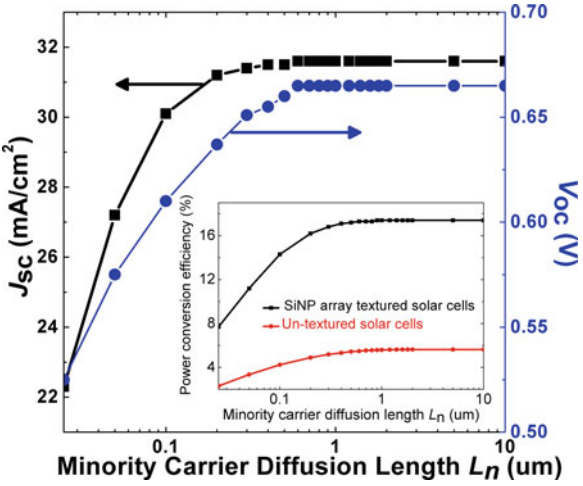

Fig. 47 Short circuit current density, J_{sc}, and open circuit voltage, V_{oc}, of the solar cell with the 1000 nm long Si-NW array (P: 500 nm; D: 250 nm) and an 800 nm thick Si film as a function of the minority carrier (electron) diffusion length, L_n. The *inset* shows the predicted PCE. The data of the thin film solar cells having the thickness of 1800 nm without texturing serve as the reference

regions, respectively [108, 109]. The illumination condition is AM 1.5G, i.e., $\sim$100 mW/cm^2. The carrier generation rate (G) under illumination is expressed by the following formula (6) [110]:

$$G = \frac{1}{2\hbar\omega}\mathrm{re}\{\nabla \cdot \mathbf{P}\} = \frac{\varepsilon_i |\mathbf{E}|^2}{2\hbar}, \tag{6}$$

where $\mathbf{P}$ is the Poynting vector, $\mathbf{E}$ is the electric field, $\hbar$ is the reduced Plank constant, ω is the angular frequency, ε_i is the imaginary part of the material's permittivity. It is noted that Eq. 6 applies to photons with the energies greater than E_g. For the photons with energies below E_g, there is no carrier generation.

Figure 47 depicts the J_{sc} and V_{oc} of the Si-NWs-textured thin film-based solar cells as a function of the minority carrier (electron) diffusion length, L_n. The doping concentration in the n$^+$ thin layer (50 nm) was set to 10^{20} cm^{-3}. It is clear that both J_{sc} and V_{oc} increase with increasing L_n, and become saturated when L_n is above $\sim$0.5 μm. The predicted PCE is summarized in the inset of Fig. 47, and also compared with that of the Si thin film solar cells having the same thickness of 1800 nm without surface texturing. Corresponding to the dramatically enhanced light absorption of the Si-NWs-textured thin film solar cells, the predicted PCE of $\sim$17.3% is achievable when $L_n = 0.6\,\mu$m, much larger than the value of $\sim$5.62% for the Si thin film solar cell with L_n of 1.4 μm. Another interesting point is that the PCE of the thin film solar cells without texturing saturates when L_n exceeds $\sim$1.2 μm, larger than the value of $\sim$0.5 μm. This indicates that the intense light absorption in the Si-NWs-textured solar cell is much closer to the top surface as compared to the case of the devices without texturing, which in the meanwhile facilitates the extraction of the minority carriers by the top electrode.

The open circuit voltage and PCE at different emitter doping concentrations are summarized in Fig. 48. The width of the emitter is held constant at 50 nm and the

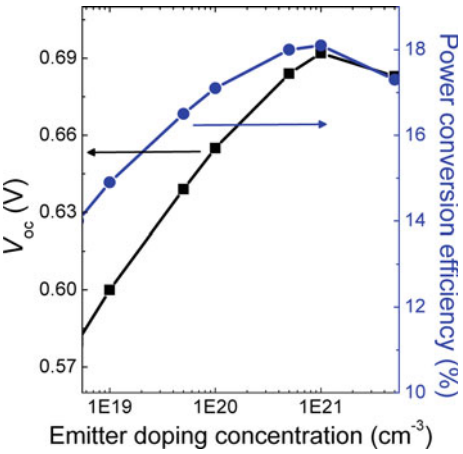

Fig. 48 V_{oc} and PCE of solar cells with a 1000 nm long Si-NW array (*P*: 500 nm; *D*: 250 nm) and an 800 nm thick underlying Si film as a function of the emitter dopant concentration, N_D

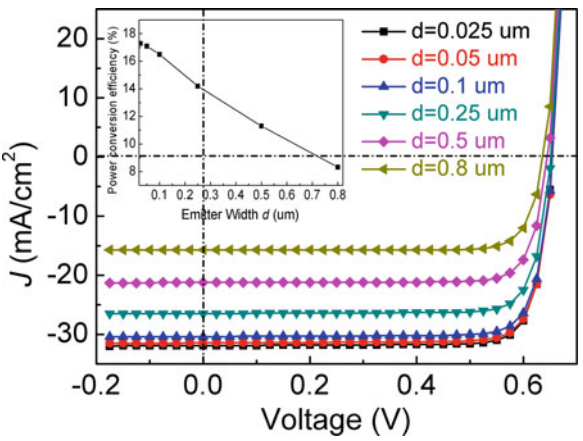

Fig. 49 *J–V* characteristics of a solar cell with the 1000 nm long Si-NWs in an array (*P*: 500 nm; *D*: 250 nm) and an 800 nm thick underlying Si film as a function of emitter width, *d*

minority-electron diffusion length of 0.6 μm is used. As depicted in Fig. 48, the V_{oc} first increases due to the widened Fermi level difference in the p–n junction with the increase of N_D. When N_D is above 10^{21} cm^{-3}, the V_{oc} then decreases due to increased carrier recombination stemming from enhanced Auger recombination. The predicted PCE shows the similar change trend with N_D, and a maximum of 18.1% is achieved for N_D of 10^{21} cm^{-3}. Here it is worth noting that for practical operation, it is difficult to achieve such a high doping concentration, and hence the emitter doping concentration of 10^{20} cm^{-3} is recommended, although there is a slight decrease of $\sim$0.8% in PCE.

Figure 49 shows the *J–V* characteristics of the Si-NWs-textured Si thin film-based solar cells with different emitter widths, *d*. The doping concentration in the emitter and the minority carrier diffusion length are fixed at 10^{20} cm^{-3} and 0.6 μm, respectively. The J_{sc} decreases with increasing *d*, especially for *d* values above

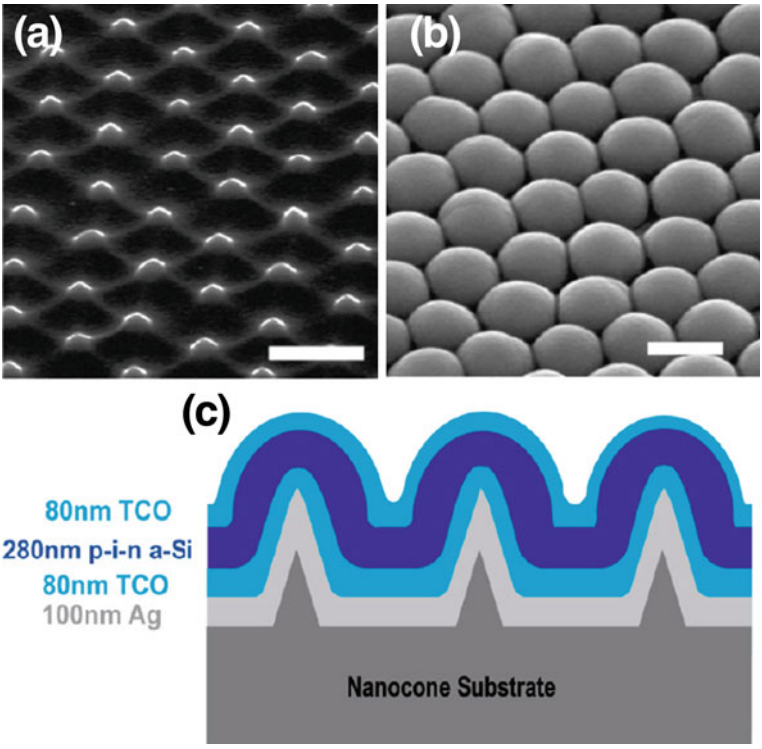

Fig. 50 Structure of the a-Si:H film-based solar cell coated onto the nanocone-textured quartz substrate. SEM images taken at 45° on **a** the nanocones array textured substrate, and **b** nanodome-shaped solar cell (the scale bar represents 500 nm). The schematic of the cross section of the solar cell is shown in (**c**). (Reprinted with permission from [112], copyright 2009, American Chemical Society)

0.1 μm, which indicates that the high-energy photons absorbed inside the emitter may not contribute to the photocurrent. This is because the photogenerated carriers fail to cross the p–n junction, and recombine in the emitter layer. The PCE and V_{oc} thus decrease with increasing d, as it is directly related to J_{sc}. Considering the practical manufacturing issues, emitter width between 0.05 and 0.1 μm is thus recommended.

From the above discussion, the conclusion can be drawn that the Si nano-structure-textured thin film solar cells are superior in both light absorption and carrier collection, compared to their thin film counterparts. Here it is also worth mentioning that for high PCE in this type of solar cell, minimizing the surface defect density is critical. As calculated, the predicted PCE for the optimized structure decreases from 17.3 to 15.2%, and further to 6.1% when increasing the surface recombination velocity from 1 to 10^3 and further to 10^5 cm/s [111].

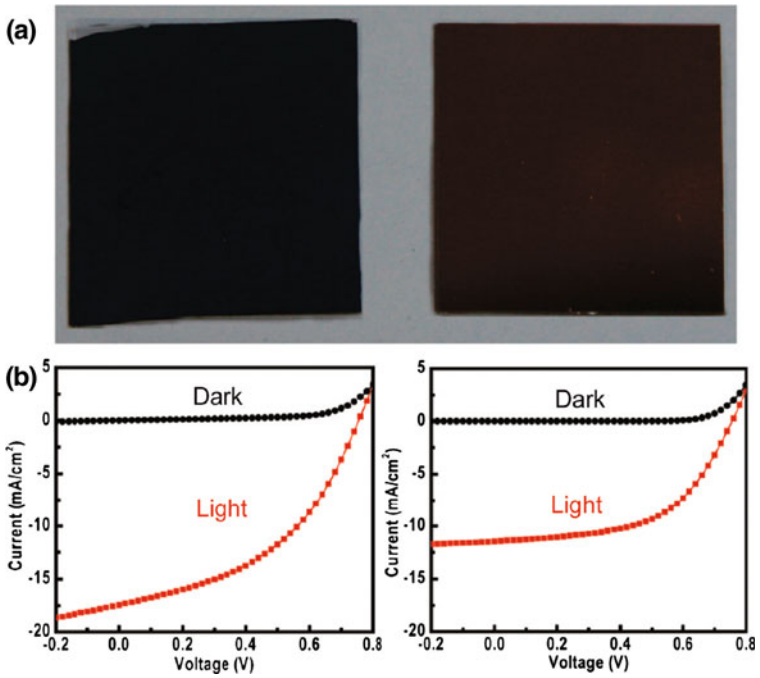

Fig. 51 **a** Photographs, and **b** dark and illuminated (AM 1.5G) *J–V* characteristics of the nanocones array incorporated solar cell (*left*) and the reference flat solar cell (*right*). (Reprinted with permission from [112], copyright 2009, American Chemical Society)

2.3.3 Research Status of Si Thin Film Solar Cells Textured with Si Nanostructures

Motivated by the excellent light trapping capability and efficient photogenerated carrier collection, Si nanostructure-textured Si thin film-based solar cells have attracted much attention. Figure 50 shows the structure of an a-Si:H film-based solar cell coated onto a NC-textured quartz substrate, fabricated by RIE using the SiO_2 nanosphere Langmuir–Blodgett monolayer mask [112]. The NCs (Fig. 50a) have base diameters of 100 nm, heights of 150 nm, and form an array with a periodicity of 450 nm. Figure 50b shows the solar cell morphology after depositing a 100 nm thick Ag back reflector, 80 nm thick TCO, 280 nm thick n–i–p a-Si:H cell (the thicknesses of the n, i and p layer are 20, 250 and 10 nm, respectively), and another 80 nm thick TCO layer onto the NCs in sequence. Figure 50c shows the cross-section of the solar cell.

Owing to the NC-textured substrate, the solar cell demonstrates superb ght absorption compared to the planar devices, which is clear from the darker appearance shown in Fig. 51a. From the *J–V* measurements (see Fig. 51b), the NC array-based solar cells can achieve a record high J_{sc} of $\sim$17.5 mA/cm^2 [113], although the contact and junction of the device were not optimized as observed

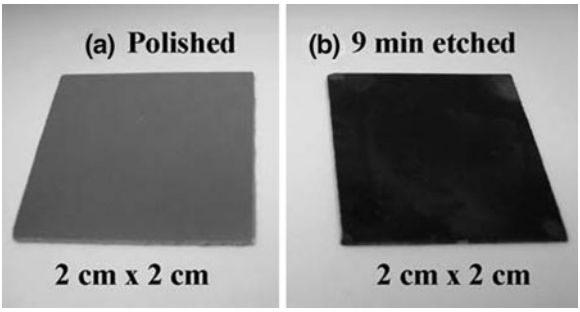

Fig. 52 Photographs of the samples **a** without and **b** with the Si-NH texturing. (Reprinted from Nishioka et al. [114], copyright 2009, with permission from Elsevier)

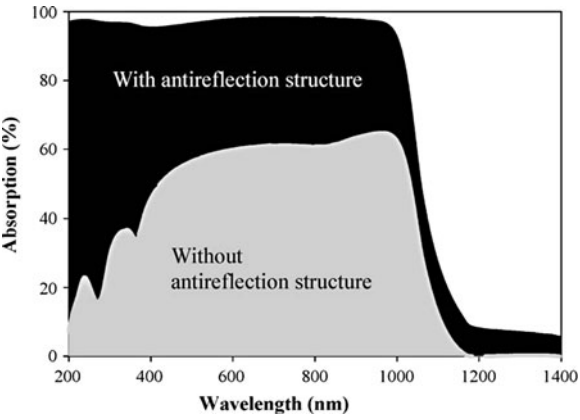

Fig. 53 Absorption spectra of the samples corresponding to those shown in Fig. 52. (Reprinted from Nishioka et al. [114], copyright 2009, with permission from Elsevier)

from the *J–V* curve shape. On the other hand, the J_{sc} of the reference solar cell is only $\sim$11.4 mA/cm^2, owing to its relatively poor light trapping capability. The reported PCE for the NC array-based solar cell is 5.9% (V_{oc}: 750 mV; FF: 0.45), which is $\sim$25% higher than that of the reference flat solar cell (PCE $\sim$4.7% with V_{oc} of 760 mV and FF of 0.54).

Nishioka et al. reported solar cells with the surface textured by Si-NH arrays, where the arrays were fabricated by immersing Ag nanoparticle (3–5 nm in diameter) coated Si in a HF/H_2O_2 solution [114]. Figure 52 shows photographs of the samples with and without the Si-NH array. The dark appearance for the etched sample indicates significantly suppressed light reflection. Corresponding to the efficient antireflection, the absorption in the Si-NH-textured sample is greatly enhanced, as shown in Fig. 53. The *J–V* measurements at AM 1.5G show that the sample textured by the Si-NH array has a J_{sc} of $\sim$31.25 mA/cm^2, much larger compared to $\sim$24.94 mA/cm^2 for the device without surface texturing. Here it is noted that the FF decreased to 0.557 from 0.596 after texturing, which can be attributed to poor electrical contact.

Recently, a research group from National Renewable Energy Laboratory developed Si-NH surface texturing by directly immersing the sample into a Au-containing solution (0.4 mM $HAuCl_4$ plus a mixture of HF, H_2O_2 and

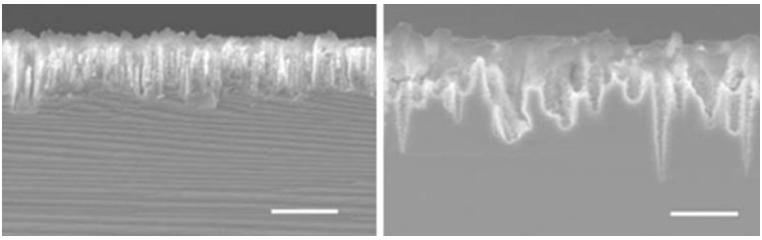

Fig. 54 Cross-sectional SEM images of the Si-NH-textured samples with etching durations of 3 min (*left*), and 6 min (*right*). The scale bar denotes 500 nm. (Reprinted with permission from [10], copyright 2009, American Institute of Physics)

H_2O (1:5:2)) [10]. Figure 54 shows the cross-sectional SEM images of the samples with etching durations of 3 min (left) and 6 min (right). The Si nanoholes were randomly distributed on the substrate surface. The optical measurement indicates that the light reflection is close to zero in the range from 350 to 1000 nm. Excellent light absorption is suggested by the high resulting PCE of $\sim$16.8% (V_{oc}: 612 mV; J_{sc}: 34.1 mA/cm^2; FF: 0.806) for the sample after introducing the Si-NH texturing, which is higher than the PCE of 13.9% for the solar cell without an antireflection coating.

Finally, we would like to point out a pressing concern that needs to be addressed for Si nanostructure-textured Si thin film-based solar cells. A high surface defect density can be created during the etching process when fabricating the nanostructures, which can severely affect the performance of the resulting solar cells. Furthermore, a rough surface on the nanostructure makes it difficult to deposit the top transparent electrode in the conformal manner necessary for efficiently collecting the photogenerated carriers.

3 Summary

In this chapter, Si nanostructure-based solar cells including Si-ND, Si-NWs and Si nanostructure-textured (Si-NWs, Si-NCs, and Si-NHs) Si thin film-based solar cells have been discussed in terms of the structure/device preparation, optical and electrical characteristics, and latest device research status. Excellent photon management is the key advantage for these solar cells compared to their planar counterparts, such as Si wafer and thin film solar cells. Preparation of high-quality nanomaterials and structures suitable for solar cells has been greatly assisted by the recent developments in nanofabrication technologies. To obtain high-efficiency Si nanostructure-based solar cells, the bottleneck is on collecting the photogenerated carriers, which relies on high-quality electrical contacts and junctions.

References

1. Würfel P (2005) Physics of solar cells: from principles to new concepts. Wiley-VCH, Weinheim
2. Pagliaro M, Palmisano G, Ciriminna R (2008) Flexible solar cells. Wiley-VCH, Weinheim
3. Green MA (2001) Third generation photovoltaics: ultra-high conversion efficiency at low cost. Prog Photovolt Res Appl 9:123–135
4. Green MA (2003) Third generation photovoltaics: advanced solar energy conversion. Springer, Berlin
5. Green MA (2002) Third generation photovoltaics: solar cells for 2020 and beyond. Physica E 14:65–70
6. Conibeer G, Green MA, Corkish R et al (2006) Silicon nanostructures for third generation photovoltaic solar cells. Thin Solid Films 511:654–662
7. Conibeer G, Green MA, Cho EC et al (2008) Silicon quantum dot nanostructures for tandem photovoltaic cells. Thin Solid Films 516:6748–6756
8. Kayes BM, Atwater HA, Lewis NS (2005) Comparison of the device physics principles of planar and radial p–n junction nanorod solar cells. J Appl Phys 97:114302-11
9. Zhu J, Yu Z, Burkhard GF et al (2009) Optical absorption enhancement in amorphous silicon nanowire and nanocone array. Nano Lett 9:279–282
10. Yuan HC, Yost VE, Page MR et al (2009) Efficient black silicon solar cell with a density-graded nanoporous surface: optical properties, performance limitations, and design rules. Appl Phys Lett 95:123501-3
11. Kim TW, Cho CH, Kim BH et al (2006) Quantum confinement effect in crystalline silicon quantum dots in silicon nitride grown using SiH_4 and NH_3. Appl Phys Lett 88:123102-3
12. van Buuren T, Dinh LN, Chase LL et al (1998) Changes in the electronic properties of Si nanocrystals as a function of particle size. Phys Rev Lett 80:3803–3806
13. Tian B, Zheng X, Kempa TJ et al (2007) Coaxial silicon nanowires as solar cells and nanoelectronic power sources. Nature 449:885–890
14. Zacharias M, Heitmann J, Scholz R et al (2002) Size-controlled highly luminescent silicon nanocrystals: A SiO/SiO_2 superlattice approach. Appl Phys Lett 80:661–663
15. Scardera G, Puzzer T, Conibeer G et al (2008) Fourier transform infrared spectroscopy of annealed silicon-rich silicon nitride films. J Appl Phys 104:104310-7
16. Song D, Cho EC, Conibeer G et al (2007) Fabrication and electrical characteristics of Si nanocrystal/*c*-Si heterojunctions. Appl Phys Lett 91:123510-3
17. Kayes BM, Filler MA, Putnam MC et al (2007) Growth of vertically aligned Si wire array over large areas (>1 cm^2) with Au and Cu catalysts. Appl Phys Lett 91:103110-3
18. Stelzner T, Pietsch M, Andrä G et al (2008) Silicon nanowire-based solar cells. Nanotechnology 19:295203-4
19. Hsu CM, Connor ST, Tang MX et al (2008) Wafer-scale silicon nanopillars and nanocones by Langmuir–Blodgett assembly and etching. Appl Phys Lett 93:133109-3
20. Hsu CH, Lo HC, Chen CF et al (2004) Generally applicable self-masked dry etching technique for nanotip array fabrication. Nano Lett 4:471–475
21. Huang MJ, Yang CR, Chiou YC et al (2008) Fabrication of nanoporous antireflection surfaces on silicon. Sol Energy Mater Sol Cells 92:1352–1357
22. Branz HM, Yost VE, Ward S et al (2009) Nanostructured black silicon and the optical reflectance of graded-density surfaces. Appl Phys Lett 94:231121-3
23. Conibeer G (2007) Third-generation photovoltaics. Mater Today 10:42–50
24. Conibeer G, Ekins-Daukes N, Guillemoles JF et al (2009) Progress on hot carrier cells. Sol Energy Mater Sol Cells 93:713–719
25. Boutry GA (1948) Augustin Fresnel: his time, life and work 1788–1827. Sci Prog 36:587–604
26. Xi JQ, Schubert MF, Kim JK et al (2007) Optical thin-film materials with low refractive index for broadband elimination of Fresnel reflection. Nat Photon 1:176–179

27. Arndt RA, Allison JF, Haynos JG et al (1975) Optical properties of the COMSAT non-reflective cell. In: Proceedings of 11th IEEE photovoltaic specialists conference, Scottsdale, May, pp 40–43
28. Zhao J, Wang A, Green MA et al (1998) 19.8% efficient "honeycomb" textured multicrystalline and 24.4% monocrystalline silicon solar cells. Appl Phys Lett 73:1991–1993
29. Green MA (2009) The path to 25% silicon solar cell efficiency: history of silicon cell evolution. Prog Photovolt Res Appl 17:183–189
30. Li JS, Yu HY, Wong SM et al (2009) Si nanopillar array optimization on Si thin films for solar energy harvesting. Appl Phys Lett 95:033102-3
31. Li JS, Yu HY, Wong SM et al (2009) Surface nanostructure optimization for solar energy harvesting in Si thin film based solar cells. In: IEEE technical digest, international electron devices meeting, pp 547–550
32. Iacona F, Franzò G, Spinella C (2000) Correlation between luminescence and structural properties of Si nanocrystals. J Appl Phys 87:1295–1303
33. Tsybeskov L, Hirschman KD, Duttagupta SP et al (1998) Nanocrystalline-silicon superlattice produced by controlled recrystallization. Appl Phys Lett 72:43–45
34. Zhang RJ, Chen YM, Lu WJ (2009) Influence of nanocrystal size on dielectric functions of Si nanocrystals embedded in SiO_2 matrix. Appl Phys Lett 95:161109-3
35. Kim TY, Park NM, Kim KH et al (2004) Quantum confinement effect of silicon nanocrystals *in situ* grown in silicon nitride films. Appl Phys Lett 85:5355–5357
36. Park NM, Choi CJ, Seong TY et al (2001) Quantum confinement in amorphous silicon quantum dots embedded in silicon nitride. Phys Rev Lett 86:1355–1357
37. Boer KW (1990) Survey of semiconductor physics. van Nostrand Reinhold, New York
38. Jiang CW, Green MA (2006) Silicon quantum dot superlattices: modeling of energy bands, densities of states, and mobilities for silicon tandem solar cell applications. J Appl Phys 99:114902-7
39. Meillaud F, Shah A, Droz C et al (2006) Efficiency limits for single-junction and tandem solar cells. Sol Energy Mater Sol Cells 90:2952–2959
40. Song D, Cho EC, Conibeer G et al (2008) Structural, electrical and photovoltaic characterization of Si nanocrystals embedded SiC matrix and Si nanocrystals/*c*-Si heterojunction devices. Sol Energy Mater Sol Cells 92:474–481
41. Cho EC, Park S, Hao X et al (2008) Silicon quantum dot/crystalline silicon solar cells. Nanotechnology 19:245201-5
42. Stupca M, Alsalhi M, Saud TA et al (2007) Enhancement of polycrystalline silicon solar cells using ultrathin films of silicon nanoparticle. Appl Phys Lett 91:063107-3
43. Kim SK, Cho CH, Kim BH et al (2009) Electrical and optical characteristics of silicon nanocrystal solar cells. Appl Phys Lett 95:143120-3
44. Perez-Wurfl I, Hao X, Gentle A et al (2009) Si nanocrystal p–i–n diodes fabricated on quartz substrates for third generation solar cell applications. Appl Phys Lett 95:153506-3
45. Cantele G, Degoli E, Luppi E et al (2005) First-principles study of n- and p-doped silicon nanoclusters. Phys Rev B 72:113303-4
46. Erwin SC, Zu L, Haftel MI et al (2005) Doping semiconductor nanocrystals. Nature 436:91–94
47. Westwater J, Gosain DP, Tomiya S et al (1997) Growth of silicon nanowires via gold/silane vapor–liquid–solid reaction. J Vac Sci Technol B 15:554–557
48. Hochbaum AI, Fan R, He R et al (2005) Controlled growth of Si nanowire array for device integration. Nano Lett 5:457–460
49. Schmidt V, Senz S, Gösele U (2005) Diameter-dependent growth direction of epitaxial silicon nanowires. Nano Lett 5:931–935
50. Tsakalakos L, Balch J, Fronheiser J et al (2007) Strong broadband optical absorption in silicon nanowire films. J. Nanophoton 1:013552-10
51. Hochbaum AI, Chen R, Delgado RD et al (2008) Enhanced thermoelectric performance of rough silicon nanowires. Nature 451:163–168

52. Chan CK, Peng H, Liu G et al (2008) High-performance lithium battery anodes using silicon nanowires. Nat Nanotechnol 3:31–35
53. Pan C, Wu H, Wang C et al (2008) Nanowire-based high performance "micro fuel cells": one nanowire, one fuel cell. Adv Mater 20:1644–1648
54. Peng KQ, Yan YJ, Gao SP et al (2002) Synthesis of large-area silicon nanowire array via self-assembling nanoelectrochemistry. Adv Mater 14:1164–1167
55. Huang Z, Fang H, Zhu J (2007) Fabrication of silicon nanowire array with controlled diameter, length, and density. Adv Mater 19:744–748
56. Wang Y, Schmidt V, Senz S et al (2006) Epitaxial growth of silicon nanowires using an aluminium catalyst. Nat Nanotechnol 1:186–189
57. Shimizu T, Xie T, Nishikawa J et al (2007) Synthesis of vertical high-density epitaxial Si (100) nanowire array on a Si (100) substrate using an anodic aluminum oxide template. Adv Mater 19:917–920
58. Wagner RS, Ellis WC (1964) Vapor–liquid–solid mechanism of single crystal growth. Appl Phys Lett 4:89–90
59. Westwater J, Gosain DP, Usui S (1998) Si nanowires grown via the vapor–liquid–solid reaction. Phys Stat Sol (a) 165:37–42
60. Yao Y, Fan S (2007) Si nanowires synthesized with Cu catalyst. Mater Lett 61:177–181
61. Morales AM, Lieber CM (1998) A laser ablation method for the synthesis of crystalline semiconductor nanowires. Science 279:208–211
62. Ke Y, Weng X, Redwing JM et al (2009) Fabrication and electrical properties of Si nanowires synthesized by Al catalyzed vapor–liquid–solid growth. Nano Lett 9:4494–4499
63. Chen W, Ahmed H (1993) Fabrication of high aspect ratio silicon pillars of <10 nm diameter. Appl Phys Lett 63:1116–1118
64. Hadobás K, Kirsch S, Carl A et al (2000) Reflection properties of nanostructure-array silicon surfaces. Nanotechnology 11:161–164
65. Bullis WM (1966) Properties of gold in silicon. Solid-State Electron 9:143–168
66. Dabbousi BO, Murray CB, Rubner MF et al (1994) Langmuir–Blodgett manipulation of size-selected CdSe nanocrystallites. Chem Mater 6:216–219
67. Peng K, Zhang M, Lu A et al (2007) Ordered silicon nanowire array via nanosphere lithography and metal induced etching. Appl Phys Lett 90:163123-3
68. Lu Y, Xiong H, Jiang X et al (2003) Asymmetric dimers can be formed by dewetting half-shells of gold deposited on the surfaces of spherical oxide colloids. J Am Chem Soc 125:12724–12725
69. Li X, Bohn PW (2000) Metal-assisted chemical etching in HF/H_2O_2 produces porous silicon. Appl Phys Lett 77:2572–2574
70. Fuhrmann B, Leipner HS, Höche HR et al (2005) Ordered array of silicon nanowires produced by nanosphere lithography and molecular beam epitaxy. Nano Lett 5:2524–2527
71. Masuda H, Fukuda K (1995) Ordered metal nanohole array made by a two-step replication of honeycomb structures of anodic alumina. Science 268:1466–1468
72. Che G, Lakshmi BB, Fisher ER et al (1998) Carbon nanotubule membranes for electrochemical energy storage and production. Nature 393:346–349
73. Choi J, Sauer G, Nielsch K et al (2003) Hexagonally arranged monodisperse silver nanowires with adjustable diameter and high aspect ratio. Chem Mater 15:776–779
74. Mei X, Kim D, Ruda HE et al (2002) Molecular-beam epitaxial growth of GaAs and InGaAs/GaAs nanodot array using anodic Al_2O_3 nanohole array template masks. Appl Phys Lett 81:361–363
75. Nasir ME, Allsopp DWE, Bowen CR et al (2010) The fabrication of mono-domain highly ordered nanoporous alumina on a wafer scale by a guided electric field. Nanotechnology 21:105303-6
76. Jessensky O, Müller F, Gösele U (1998) Self-organized formation of hexagonal pore array in anodic alumina. Appl Phys Lett 72:1173–1175
77. Lombardi I, Hochbaum AI, Yang P et al (2006) Synthesis of high density, size-controlled Si nanowire array by porous anodic alumina mask. Chem Mater 18:988–991

78. Guo LJ (2007) Nanoimprint lithography: methods and material requirements. Adv Mater 19:495–513
79. Plass KE, Filler MA, Spurgeon JM et al (2008) Flexible polymer-embedded Si wire array. Adv Mater 21:325–328
80. Tsakalakos L, Balch J, Fronheiser J et al (2007) Silicon nanowire solar cells. Appl Phys Lett 91:233117-3
81. Garnett EC, Yang P (2008) Silicon nanowire radial p–n junction solar cells. J Am Chem Soc 130:9224–9225
82. Kalita G, Adhikari S, Aryal HR et al (2009) Silicon nanowire array/polymer hybrid solar cell incorporating carbon nanotubes. J Phys D Appl Phys 42:115104-5
83. Street RA, Qi P, Lujan R et al (2008) Reflectivity of disordered silicon nanowires. Appl Phys Lett 93:163109-3
84. Hu L, Chen G (2007) Analysis of optical absorption in silicon nanowire array for photovoltaic applications. Nano Lett 7:3249–3252
85. Air Mass 1.5 Spectra (2010) American society for testing and materials. http://rredc.nrel.gov/solar/spectra/am1.5/#1962. Accessed 9 March 2010
86. Shockley W, Queisser HJ (1961) Detailed balance limit of efficiency of p–n junction solar cells. J Appl Phys 32:510–519
87. Li JS, Yu HY, Wong SM et al (2009) Design guidelines of periodic Si nanowire array for solar cell application. Appl Phys Lett 95:243113-3
88. Putnam MC, Turner-Evans DB, Kelzenberg MD et al (2009) 10 μm minority-carrier diffusion lengths in Si wires synthesized by Cu-catalyzed vapour–liquid–solid growth. Appl Phys Lett 95:163116-3
89. Maiolo JR III, Kayes BM, Filler MA et al (2007) High aspect ratio silicon wire array photoelectrochemical cells. J Am Chem Soc 129:12346–12347
90. Sivakov V, Andrä G, Gawlik A et al (2009) Silicon nanowire-based solar cells on glass: synthesis, optical properties, and cell parameters. Nano Lett 9:1549–1554
91. van den Donker MN, Gordijn A, Stiebig H et al (2007) Flexible amorphous and microcrystalline silicon tandem solar modules in the temporary superstrate concept. Sol Energy Mater Sol Cells 91:572–580
92. Garnett E, Yang P (2010) Light trapping in silicon nanowire solar cells. Nano Lett 10:1082–1087
93. Yoon J, Baca AJ, Park SI et al (2008) Ultrathin silicon solar microcells for semitransparent, mechanically flexible and microconcentrator module designs. Nat Mater 7:907–915
94. Campbell P, Green MA (1987) Light trapping properties of pyramidally textured surfaces. J Appl Phys 62:243–249
95. Gray JL (2003) The physics of the solar cell. In: Luque A, Hegedus S (eds) Handbook of photovoltaic science and engineering. Wiley, Chichester
96. Kelzenberg MD, Turner-Evans DB, Kayes BM et al (2008) Single-nanowire Si solar cells. In: Proceedings of the 33rd IEEE photovoltaic specialists conference, pp 144–149
97. Bai XD, Zhi CY, Liu S et al (2003) High-density uniformly aligned silicon nanotip array and their enhanced field emission characteristics. Solid State Commun 125:185–188
98. Wang Q, Li JJ, Bai XD et al (2005) Field emission properties of carbon coated Si nanocone array on porous silicon. Nanotechnology 15:2919–2922
99. Hsu CH, Huang YF, Chen LC et al (2006) Morphology control of silicon nanotips fabricated by electron cyclotron resonance plasma etching. J Vac Sci Technol B 24:308–311
100. Li LP, Lu YF, Doerr DW et al (2004) Parametric investigation of laser nanoimprinting of hemispherical cavity array. J Appl Phys 96:5144–5151
101. Huang SM, Hong MH, Luk'yanchuk BS et al (2002) Pulsed laser-assisted surface structuring with optical and near-field enhanced effects. J Appl Phys 92:2495–2500
102. Tsujino K, Matsumura M, Nishimoto Y (2006) Texturization of multicrystalline silicon wafers for solar cells by chemical treatment using metallic catalyst. Sol Energy Mater Sol Cells 90:100–110

103. Gorostiza P, Díaz R, Servat J et al (1997) Atomic force microscopy study of the silicon doping influence on the first stages of platinum electroless deposition. J Electrochem Soc 144:909–914
104. Wang F, Yu HY, Wang XC et al (2010) Maskless fabrication of large scale Si nanohole array via laser annealed metal nanoparticles catalytic etching for photovoltaic application. J Appl Phys 108:024301-3
105. Li JS, Yu HY, Wong SM et al (2010) Si nanocone array optimization on crystalline Si thin films for solar energy harvesting. J Phys D Appl Phys 43:255101-7
106. Wang F, Yu HY, Li JS et al (2010) Optical absorption enhancement in nanopore textured-silicon thin film for photovoltaic application. Opt Lett 35:40–42
107. Wong SM, Yu HY, Li JS et al (2010) Design high-efficiency Si nanopillar-array-textured thin film solar cell. IEEE Electron Device Lett 31:335–337
108. Shockley W, Read WT (1952) Statistics of the recombinations of holes and electrons. Phys Rev 87:835–842
109. Shibib MA, Lindholm FA, Fossum JG (1979) Auger recombination in heavily doped shallow-emitter silicon p–n-junction solar cells, diodes and transistors. IEEE Trans Electron Devices ED 26:1104–1106
110. Kelzenberg MD, Putnam MC, Turner-Evans DB et al (2009) Predicted efficiency of Si wire array solar cells. In: Proceedings of the 34th IEEE photovoltaic specialists conference, pp 391–396
111. Li JS, Wong SM, Li YL et al (2010) High-efficiency crystalline Si thin film solar cells with Si nanopillar array textured surfaces. In: Proceedings of the 35th IEEE photovoltaic specialists conference
112. Zhu J, Hsu CM, Yu Z et al (2010) Nanodome solar cells with efficient light management and self-cleaning. Nano Lett 10:1979–1984
113. Green MA, Emery K, Hishikawa Y et al (2009) Solar cell efficiency tables (version 34). Prog Photovolt Res Appl 17:320–326
114. Nishioka K, Sueto T, Saito N (2009) Formation of antireflection nanostructure for silicon solar cells using catalysis of single nano-sized silver particle. Appl Surf Sci 255:9504–9507